

11-30-2018

Isostructural Metal-Insulator Transition in VO_2

J. W. Spinuzzi
Boise State University

D. A. Tenne
Boise State University

Title: Isostructural metal-insulator transition in VO₂

Authors: D. Lee¹, B. Chung², Y. Shi³, G.-Y. Kim⁴, N. Campbell⁵, F. Xue³, K. Song⁴, S.-Y. Choi⁴, J. P. Podkaminer¹, T. H. Kim¹, P. J. Ryan^{6,7}, J.-W. Kim⁶, T. R. Paudel⁸, J.-H. Kang¹, J. W. Spinuzzi⁹, D. A. Tenne⁹, E. Y. Tsymbal⁸, M. S. Rzchowski⁵, L. Q. Chen³, J. Lee^{2*}, C. B. Eom^{1*}

Affiliations:

¹Department of Materials Science and Engineering, University of Wisconsin–Madison, Madison, Wisconsin 53706, USA.

²School of Advanced Materials Science and Engineering, Sungkyunkwan University, Suwon 16419, Korea.

³Department of Materials Science and Engineering, Pennsylvania State University, University Park, Pennsylvania 16802, USA.

⁴Department of Materials Modeling and Characterization, Korea Institute of Materials Science, Changwon 642-831, Korea.

⁵Department of Physics, University of Wisconsin–Madison, Madison, Wisconsin 53706, USA.

⁶Advanced Photon Source, Argonne National Laboratory, Argonne, Illinois 60439, USA.

⁷School of Physical Sciences, Dublin City University, Dublin 9, Ireland

⁸Department of Physics and Astronomy and Nebraska Center for Materials and Nanoscience, University of Nebraska, Lincoln–Nebraska, Nebraska 68588, USA.

⁹Department of Physics, Boise State University, Boise, Idaho 83725-1570, USA.

*Correspondence to: eom@engr.wisc.edu (C.B.E.), jclee@skku.edu (J.L.)

Abstract: The metal-insulator transition in correlated materials is usually coupled to a symmetry-lowering structural phase transition. This coupling not only complicates the understanding of the basic mechanism of this phenomenon but also limits the speed and endurance of prospective electronic devices. Here, we design and demonstrate an isostructural, purely electronically-driven metal-insulator transition in epitaxial heterostructures of an archetypal correlated material vanadium dioxide. A combination of thin-film synthesis, structural and electrical characterizations, and theoretical modeling reveals that an interface interaction suppresses the electronic correlations without changing the crystal structure in this otherwise correlated insulator. It stabilizes a non-

equilibrium metallic phase, and leads to an isostructural metal-insulator transition. This discovery will provide insights into correlated phase transitions and may aid the design of device functionalities.

Main Text:

Understanding metal-insulator transitions in strongly correlated materials is one of the major challenges in condensed matter physics (1–5), with implications for both fundamental science and technology (6, 7). Correlated materials exhibit strong coupling between charge, spin, and lattice degrees of freedom, so that the metal-insulator transition is almost always accompanied by an associated structural phase transition. This coexistence obscures the underlying physics, and makes it difficult to disentangle the different intrinsic interactions controlling the metal-insulator transition. Furthermore, the structural transition generally limits the ultimate switching speed (9, 10) and endurance (6, 11) of ultrafast electronic devices (6–8) based on the metal-insulator transition in these correlated materials. Achieving an isostructural metal-insulator transition is thus of great interest.

As a model system for this study, we choose the archetypal correlated material vanadium dioxide (VO_2) (12–27). VO_2 is metallic at high temperatures and becomes insulating near room temperature (341 K in bulk) (12); the metal-insulator transition is accompanied by a structural phase transition from the high-temperature rutile structure to the low-temperature monoclinic structure via the formation of V-V dimers along the c -axis. There has been extensive debate over whether the primary mechanism of the metal-insulator transition in VO_2 is an electron-lattice interaction (Peierls transition) (13) or an electron-electron interaction (Mott transition) (14), and it is now accepted that both Peierls and Mott physics are important (15, 16). In particular, recent

ultrafast photoexcitation experiments (21, 22) have revealed the presence of a non-equilibrium metallic monoclinic state in addition to the known bulk equilibrium phases, i.e., insulating monoclinic and metallic rutile phases. [This metallic transition in photoexcited monoclinic VO₂ could originate from the dynamically screened Coulomb interaction \(22\), assisted by an electronically one-dimensional characteristic of V-V dimers \(27\), and suggests a route for an isostructural metal-insulator transition: If the metallic monoclinic phase could be stabilized, rather than just being transient, we could achieve an isostructural metallic transition in insulating monoclinic VO₂.](#)

To this end, we consider a nanoscale bilayer consisting of two VO₂ layers with different transition temperatures (T_1 and T_2 in Fig. 1A). In this bilayer, a rutile/monoclinic heterostructure can occur at intermediate temperatures between T_1 and T_2 , in which interval the desired metallic monoclinic phase might be stabilized, e.g., via a collective carrier delocalization (19). To experimentally realize such a bilayer, we needed to achieve control over the transition temperature in a VO₂ layer; to do that, we utilized an intrinsic point defect, i.e., oxygen vacancy (29), and the resulting electron doping. Introducing a minute amount of oxygen vacancies can lower the transition temperature of VO₂ without compromising the sharp metal-insulator transition (30). By changing the oxygen partial pressure during film growth (figs. S1–S4) (28), we prepared an artificial bilayer (Fig. 1B, inset), fully coherent on TiO₂ (001) substrate, consisting of slightly oxygen-deficient VO_{2- δ} and stoichiometric VO₂ layers. [Each individual 8nm thick VO_{2- \$\delta\$} and VO₂ layers have transition temperatures of \$T_1 \sim 279\$ K and \$T_2 \sim 287\$ K, respectively \(Fig. 1A\).](#)

To visualize the oxygen vacancy profile in the bilayer, we carry out atomic-scale imaging using scanning transmission electron microscopy (STEM) (28). In STEM, the low angle annular dark field (LAADF) image is very sensitive to the strain fields from oxygen vacancies (29),

whereas the high angle annular dark field (HAADF) image is dominated by the (high-Z) cation sites. Our HAADF image (left in Fig. 1B) shows little intensity change across the $\text{VO}_{2-\delta}/\text{VO}_2$ interface (denoted by the white dashed line). In contrast, the LAADF image (right in Fig. 1B) displays a noticeable, abrupt intensity change across the $\text{VO}_{2-\delta}/\text{VO}_2$ interface, emphasizing the oxygen deficiency in the $\text{VO}_{2-\delta}$ layer. Our results show that introducing a small amount of oxygen vacancies, rather than extrinsic dopants, creates a chemically sharp interface with a sub-1-nm width (fig. S5) and leads to a quasi-homogeneous, single crystalline character of the bilayer. Electron energy loss spectroscopy (EELS) measurements (fig. S6) independently quantify the oxygen vacancy difference between the layers. Considering this nanoengineered oxygen vacancy profile, we expect two distinct transition temperatures in the top $\text{VO}_{2-\delta}$ and bottom VO_2 layers.

Using Raman spectroscopy (28), we monitored the structural phase transition in the $\text{VO}_{2-\delta}/\text{VO}_2$ bilayer (Figs. 2, A and B). With decreasing temperature, several noticeable Raman peaks (e.g., ω_1 , ω_2 , and ω_3 peaks in Fig. 2A) arise suddenly from the monoclinic distortions during the structural transition (31, 32). Our quantitative analysis (Fig. 2B) clearly shows the two-step structural phase transition in the $\text{VO}_{2-\delta}/\text{VO}_2$ bilayer, contrary to the single-step transition in a VO_2 single layer. Using temperature-dependent X-ray diffraction measurements (Figs. 2, C–E) (28) and phase-field simulations (fig. S14), we furthermore confirm the two-step structural phase transition in the bilayer. This two-step structural phase transition can be explained by two separate structural transitions, i.e., at $T \sim 279$ K for the top $\text{VO}_{2-\delta}$ layer and at $T \sim 287$ K for the bottom VO_2 layer. At intermediate temperatures between $T \sim 279$ K and 287 K (as shown by green color in Figs. 2B and E), the top $\text{VO}_{2-\delta}$ and bottom VO_2 layers have rutile and monoclinic structures, respectively, which forms the desired rutile/monoclinic heterostructure (Fig. 2B, inset).

We explore the electronic phase transition in the $\text{VO}_{2-\delta}/\text{VO}_2$ bilayer, by measuring the electrical resistivity (Fig. 3A) and carrier concentration (fig. S7). In stark contrast to the two-step structural transition, our bilayer shows a single-step, collective metal-insulator transition at $T \sim 279$ K. The electronic phase transition of the bilayer looks nearly identical to that of a $\text{VO}_{2-\delta}$ single layer (black dotted line in Fig. 3A), which means that in the $\text{VO}_{2-\delta}/\text{VO}_2$ bilayer, the electronic phase (i.e., metallic or insulating) of the VO_2 layer collectively follows that of the $\text{VO}_{2-\delta}$ layer. Notably, when an ultrathin (~ 2 nm) TiO_2 layer is inserted between $\text{VO}_{2-\delta}$ and VO_2 , the $\text{VO}_{2-\delta}/\text{TiO}_2/\text{VO}_2$ system exhibits a two-step metal-insulator transition (fig. S8). This confirms the intrinsic effect of the rutile/monoclinic interface on the observed single-step, collective metal-insulator transition in the $\text{VO}_{2-\delta}/\text{VO}_2$ bilayer.

Taken together, our observation of the two-step structural and single-step electronic phase transitions unambiguously confirms the emergence of a stable metallic monoclinic phase in the $\text{VO}_{2-\delta}/\text{VO}_2$ bilayer. With the decrease in temperature, the bottom VO_2 layer exhibits the rutile-to-monoclinic structural transition at $T \sim 287$ K (Fig. 3B), but global metallicity of the whole bilayer remains unchanged (Fig. 3A and fig. S7). This is consistent with the explanation that, when interfaced with the metallic rutile $\text{VO}_{2-\delta}$ layer, the bottom VO_2 layer becomes a stable metallic monoclinic phase. This interface-induced bulk carrier delocalization (19) plays a decisive role in the single-step metal-insulator transition. Importantly, Fig. 3C shows little change in the peak positions of ω_2 and ω_3 , attributed to the ionic motion of V-V dimers (23, 32), during the metal-insulator transition at ~ 279 K. This directly illustrates the isostructural metal-insulator transition without any crystalline structure change at ~ 279 K in the bottom stoichiometric VO_2 layer.

To further understand the emergence of isostructural metal-insulator transition, we carry out theoretical modeling of the rutile/monoclinic heterostructure. First, we perform non-spin-

polarized density functional theory (DFT) calculations (28) with Hubbard U correction for properly predicting the insulating monoclinic ground state in bulk VO_2 (33). The calculated density of states of the heterostructure (Fig. 4A) manifests the metallic nature in the monoclinic region (Fig. 4B and fig. S10), consistent with our experimental observation (Fig. 3). Inside the monoclinic region, the electronic structure is strongly modified, resulting in significant band gap narrowing. This is largely driven by hole doping of the monoclinic region (fig. S12), stemming from the different work functions of the rutile and monoclinic phases (34). Such a hole doping reduces electronic correlations, causing a complete collapse of the band gap in monoclinic VO_2 (22). Simultaneously, from the DFT results, we infer that the rutile/monoclinic heterostructure has a very small interfacial energy (28), which may also play a role in stabilizing the metallic monoclinic phase.

To explore the effects of electronic correlations and interfacial energy, we use a generalized Landau thermodynamic approach implemented in phase-field modeling (28). The Landau potential incorporates two different order parameters, η_s describing the structural transition [i.e., from rutile ($\eta_s = 0$) to monoclinic ($\eta_s = 1$) phase] and η_{EC} describing the electronic correlations, which controls metal-insulator transition [i.e., from metal ($\eta_{EC} = 0$) to insulator ($\eta_{EC} = 1$)]. We find only two bulk equilibrium phases, i.e., the metallic rutile phase with little electronic correlation ($\eta_s = \eta_{EC} = 0$) at high temperatures and the correlated insulating monoclinic phase ($\eta_s = \eta_{EC} = 1$) at low temperatures (fig. S13). However, in addition to these bulk equilibrium phases, we predict the presence of a non-equilibrium metallic monoclinic phase with suppressed correlation ($\eta_s = 1$ and $\eta_{EC} = 0$), as represented by the local minimum in the energy landscape just below the transition temperature (Fig. 4C).

We now employ phase-field modeling to investigate phase stabilities in the experimentally studied rutile/monoclinic heterostructure. Figure 4D shows the total energy of the rutile/monoclinic heterostructure, as a function of the thickness t_m of the monoclinic layer. The interfacial energy between metallic rutile and metallic monoclinic phases is naturally smaller than that between metallic rutile and insulating monoclinic phases in the phase-field model, owing to the homogeneous η_{EC} in the former case (28). When t_m is below critical thickness t_c , the interfacial energy contribution dominates over the bulk energy contribution, and as a result, the metallic monoclinic phase with suppressed correlation (i.e., $\eta_{EC} = 0$) becomes energetically preferred and stabilized (fig. S14). It is noteworthy that our experimental and theoretical results have consistently demonstrated the isostructural metal-insulator transition in device-relevant thin-film geometries of genuine VO₂, without necessity of specific conditions, such as non-equilibrium condition (21–24) or surface state (5, 25). Stabilizing the monoclinic structure through our bilayer approach separates the electronic and structural phase transitions, in contrast to previous reports (35, 36).

There has been a growing interest in non-equilibrium states in correlated materials (21, 22, 37), because of the opportunity to discover exotic physics not exhibited in equilibrium. Ultrafast spectroscopies have been mainly used for exploring non-equilibrium states; our study paves a way to stabilize and explore the non-equilibrium phase (e.g., metallic monoclinic state in VO₂) in a controlled way. As VO₂ is a simple spin-1/2 system with one d electron (38), it will be intriguing to study the spin and orbital physics in the stabilized metallic monoclinic phase. We anticipate that our approach for artificial stabilization of non-equilibrium states will be generally applicable to correlated materials, so that a variety of unconventional phenomena can be designed through heterostructure engineering.

References and Notes:

1. M. Imada, A. Fujimori, Y. Tokura, Metal-insulator transitions. *Rev. Mod. Phys.* **70**, 1039–1263 (1998).
2. M. Uehara, S. Mori, C. H. Chen, S.-W. Cheong, Percolative phase separation underlies colossal magnetoresistance in mixed-valent manganites. *Nature* **399**, 560–563 (1999).
3. L. Zhang, C. Israel, A. Biswas, R. L. Greene, A. De Lozanne, Direct observation of percolation in a manganite thin film. *Science* **298**, 805–807 (2002).
4. E. Dagotto, Complexity in strongly correlated electronic Systems. *Science* **309**, 257–262 (2005).
5. R. G. Moore, J. Zhang, V. B. Nascimento, R. Jin, J. Guo, G. T. Wang, Z. Fang, D. Mandrus, E. W. Plummer, A Surface-Tailored, Purely Electronic, Mott Metal-to-Insulator Transition. *Science*, **318**, 615–619 (2007).
6. Z. Yang, C. Ko, S. Ramanathan, Oxide electronics utilizing ultrafast metal-insulator transitions. *Ann. Rev. Mater. Res.* **41**, 337–367 (2011).
7. D. M. Newns, J. A. Misewich, C. C. Tsuei, A Gupta, B. A. Scott, A. Schrott, Mott transition field effect transistor. *Appl. Phys. Lett.* **73**, 780–782 (1998).
8. Y. Zhou, S. Ramanathan, Mott memory and neuromorphic devices. *Proc. IEEE* **103**, 1289–1310 (2015).
9. A. Cavalleri, Th. Dekorsy, H. H. W. Chong, J. C. Kieffer, R. W. Schoenlein, Evidence for a structurally-driven insulator-to-metal transition in VO₂: A view from the ultrafast timescale. *Phys. Rev. B* **70**, 161102(R) (2004).
10. P. Baum, D.-S. Yang, A. H. Zewail, 4D visualization of transitional structures in phase transformations by electron diffraction. *Science* **318**, 788–792 (2007).
11. D. Maurer, A. Leue, Investigation of transition metal oxides by ultrasonic microscopy. *Mater. Sci. Eng. A* **370**, 440–443 (2004).
12. F. J. Morin, Oxides which show a metal-to-insulator transition at the Neel temperature. *Phys. Rev. Lett.* **3**, 34–36 (1959).
13. R. M. Wentzcovitch, W. W. Schulz, P. B. Allen, VO₂: Peierls or Mott-Hubbard? A view from band theory. *Phys. Rev. Lett.* **72**, 3389–3392 (1994).
14. T. M. Rice, H. Launois, J. P. Pouget, Comment on “VO₂: Peierls or Mott-Hubbard? A view from band theory”. *Phys. Rev. Lett.* **73**, 3042 (1994).
15. S. Biermann, A. Poteryaev, A. I. Lichtenstein, A. Georges, Dynamical singlets and correlation-assisted Peierls transition in VO₂. *Phys. Rev. Lett.* **94**, 026404 (2005).
16. M. W. Haverkort, Z. Hu, A. Tanaka, W. Reichelt, S. V. Streltsov, M. A. Korotin, V. I. Anisimov, H. H. Hsieh, H.-J. Lin, C. T. Chen, D. I. Khomskii, L. H. Tjeng, Orbital-assisted metal-insulator transition in VO₂. *Phys. Rev. Lett.* **95**, 196404 (2005).
17. M. M. Qazilbash, M. Brehm, B.-G. Chae, P.-C. Ho, G. O. Andreev, B.-J. Kim, S. J. Yun, A. V. Balatsky, M. B. Maple, F. Keilmann, H.-T. Kim, D. N. Basov, Mott transition in VO₂ revealed by infrared spectroscopy and nano-imaging. *Science* **318**, 1750–1753 (2007).

18. M. Liu, H. Y. Hwang, H. Tao, A. C. Strikwerda, K. Fan, G. R. Keiser, A. J. Sternbach, K. G. West, S. Kittiwatanakul, J. Lu, S. A. Wolf, F. G. Omenetto, X. Zhang, K. A. Nelson, R. D. Averitt, Terahertz-field-induced insulator-to-metal transition in vanadium dioxide metamaterial. *Nature* **487**, 345–348 (2012).
19. M. Nakano, K. Shibuya, D. Okuyama, T. Hatano, S. Ono, M. Kawasaki, Y. Iwasa, Y. Tokura, Collective bulk carrier delocalization driven by electrostatic surface charge accumulation. *Nature* **487**, 459–462 (2012).
20. J. Jeong, N. Aetukuri, T. Graf, T. D. Schladt, M. G. Samant, S. S. P. Parkin, Suppression of metal-insulator transition in VO₂ by electric field-induced oxygen vacancy formation. *Science* **339**, 1402–1405 (2013).
21. V. R. Morrison, R. P. Chatelain, K. L. Tiwari, A. Hendaoui, A. Bruhács, M. Chaker, B. J. Siwick, A photoinduced metal-like phase of monoclinic VO₂ revealed by ultrafast electron diffraction. *Science* **346**, 445–448 (2014).
22. D. Wegkamp, M. Herzog, L. Xian, M. Gatti, P. Cudazzo, C. L. McGahan, R. E. Marvel, R. F. Haglund, Jr., A. Rubio, M. Wolf, J. Stähler, Instantaneous band gap collapse in photoexcited monoclinic VO₂ due to photocarrier doping. *Phys. Rev. Lett.* **113**, 216401 (2014).
23. E. Arcangeletti, L. Baldassarre, D. Di Castro, S. Lupi, L. Malavasi, C. Marini, A. Perucchi, and P. Postorino, Evidence of a pressure-induced metallization process in monoclinic VO₂. *Phys. Rev. Lett.* **98**, 196406 (2007).
24. Z. Tao, T.-R. T. Han, S. D. Mahanti, P. M. Duxbury, F. Yuan, C.-Y. Ruan, K. Wang, J. Wu, Decoupling of structural and electronic phase transitions in VO₂. *Phys. Rev. Lett.* **109**, 166406 (2012).
25. J. Laverock, S. Kittiwatanakul, A. A. Zakharov, Y. R. Niu, B. Chen, S. A. Wolf, J. W. Lu, K. E. Smith, Direct observation of decoupled structural and electronic transitions and an ambient pressure monocliniclike metallic phase of VO₂. *Phys. Rev. Lett.* **113**, 216402 (2014).
26. J. D. Budai, J. Hong, M. E. Manley, E. D. Specht, C. W. Li, J. Z. Tischler, D. L. Abernathy, A. H. Said, B. M. Leu, L. A. Boatner, R. J. McQueeney, O. Delaire, Metallization of vanadium dioxide driven by large phonon entropy. *Nature* **515**, 535–539 (2014).
27. V. Eyert, The metal-insulator transitions of VO₂: A band theoretical approach. *Ann. Phys.* **11**, 650–704 (2002).
28. Materials and methods are available as supplementary materials on Science Online.
29. D. A. Muller, N. Nakagawa, A. Ohtomo, J. L. Grazul, H. Y. Hwang, Atomic-scale imaging of nanoengineered oxygen vacancy profiles in SrTiO₃. *Nature* **430**, 657–661 (2004).
30. C. H. Griffiths, H. K. Eastwood, Influence of stoichiometry on the metal-semiconductor transition in vanadium dioxide. *J. Appl. Phys.* **45**, 2201–2206 (1974).
31. R. Srivastava, L. L. Chase, Raman spectrum of semiconducting and metallic VO₂. *Phys. Rev. Lett.* **27**, 727–730 (1971).
32. L. Bai, Q. Li, S. A. Corr, Y. Meng, C. Park, S. V. Sinogeikin, C. Ko, J. Wu, G. Shen, Pressure-induced phase transitions and metallization in VO₂. *Phys. Rev. B* **91**, 104110 (2015).

33. X. Yuan, Y. Zhang, T. A. Abtew, P. Zhang, W. Zhang, VO₂: Orbital competition, magnetism, and phase stability. *Phys. Rev. B* **86**, 235103 (2012).
34. C. Ko, Z. Yang, S. Ramanathan, Work function of vanadium dioxide thin films across the metal-insulator transition and the role of surface nonstoichiometry. *ACS Appl. Mater. Interfaces* **3**, 3396–3401 (2011).
35. M. Yang, Y. Yang, B. Hong, L. Wang, K. Hu, Y. Dong, H. Xu, H. Huang, J. Zhao, H. Chen, L. Song, H. Ju, J. Zhu, J. Bao, X. Li, Y. Gu, T. Yang, X. Gao, Z. Luo, C. Gao, Suppression of structural phase transition in VO₂ by epitaxial strain in vicinity of metal-insulator transition. *Sci. Rep.* **6**, 23119 (2016).
36. The supplementary X-ray data in (35) indicates that a structural transition remains.
37. J. Kim, X. Hong, C. Jin, S.-F. Shi, C.-Y. S. Chang, M.-H. Chiu, L.-J. Li, F. Wang, Ultrafast generation of pseudo-magnetic field for valley excitons in WSe₂ monolayers. *Science* **346**, 1205–1208 (2014).
38. H. He, A. X. Gray, P. Granitzka, J. W. Jeong, N. P. Aetukuri, R. Kukreja, Lin Miao, S. A. Breitweiser, J. Wu, Y. B. Huang, P. Olalde-Velasco, J. Pelliciari, W. F. Schlotter, E. Arenholz, T. Schmitt, M. G. Samant, S. S. P. Parkin, H. A. Dürr, L. A. Wray, Measurement of collective excitations in VO₂ by resonant inelastic x-ray scattering. *Phys. Rev. B* **94**, 161119(R) (2016).
39. L. Q. Jiang, J. K. Guo, H. B. Liu, M. Zhu, X. Zhou, P. Wu, C. H. Li, Prediction of lattice constant in cubic perovskites. *J. Phys. Chem. Solids* **67**, 1531–1536 (2006).
40. D. Marrocchelli, S. R. Bishop, H. L. Tuller, B. Yildiz, B. Understanding chemical expansion in non-stoichiometric oxides: ceria and zirconia case studies. *Adv. Funct. Mater.* **22**, 1958–1965 (2012).
41. R. D. Shannon, Revised effective ionic radii and systematic studies of interatomic distances in halides and chalcogenides. *Acta Crystallogr., Sect. A* **32**, 751–767 (1976).
42. S. Hillyard, J. Silcox, Detector geometry, thermal diffuse scattering and strain effects in ADF STEM imaging. *Ultramicroscopy* **58**, 6–17 (1995).
43. S.-Y. Choi, S.-D. Kim, M. Choi, H.-S. Lee, J. Ryu, N. Shibata, T. Mizoguchi, E. Tochigi, T. Yamamoto, S.-J. L. Kang, Y. Ikuhara, Assessment of strain-generated oxygen vacancies using SrTiO₃ bicrystals. *Nano Lett.* **15**, 4129–4134 (2015).
44. P. Schilbe, D. Maurer, Lattice dynamics in VO₂ near the metal-insulator transition. *Mater. Sci. Eng. A* **370**, 449 (2004).
45. G. Kresse, D. Joubert, From ultrasoft pseudopotentials to the projector augmented-wave method. *Phys. Rev. B* **59**, 1758–1775 (1999).
46. G. Kresse, J. Furthmüller, Efficient iterative schemes for ab initio total-energy calculations using a plane-wave basis set. *Phys. Rev. B* **54**, 11169–11186 (1996).
47. P. E. Blöchl, Projector augmented-wave method. *Phys. Rev. B* **50**, 17953–17979 (1994).
48. J. P. Perdew, A. Zunger, Self-interaction correction to density-functional approximations for many-electron systems. *Phys. Rev. B* **23**, 5048–5079 (1981).

49. V. I. Anisimov, F. Aryasetiawan, A. I. Lichtenstein, First-principles calculations of the electronic structure and spectra of strongly correlated systems: the LDA+ U method. *J. Phys. Condens. Matter* **9**, 767–808 (1997).
50. Z. Zhu, U. Schwingenschlögl, Comprehensive picture of VO₂ from band theory. *Phys. Rev. B* **86**, 075149 (2012).
51. S. L. Dudarev, S. Y. Savrasov, C. J. Humphreys, A. P. Sutton, Electron-energy-loss spectra and the structural stability of nickel oxide: An LSDA+U study. *Phys. Rev. B* **57**, 1505–1509 (1998).
52. C. Noguera, *Physics and chemistry at oxide surfaces* (Cambridge University Press, 1996).
53. A. M. Stoneham, Systematics of metal-insulator interfacial energies: A new rule for wetting and strong catalyst-support interactions. *Appl. Surf. Sci.* **14**, 249–259 (1983).
54. J. H. Park, J. M. Coy, T. S. Kasirga, C. Huang, Z. Fei, S. Hunter, D. H. Cobden, Measurement of a solid-state triple point at the metal-insulator transition in VO₂. *Nature* **500**, 431–434 (2013).
55. J. Wu, Q. Gu, B. S. Guiton, N. P. de Leon, L. Ouyang, H. Park, Strain-induced self organization of metal-insulator domains in single-crystalline VO₂ nanobeams. *Nano Lett.* **6**, 2313–2317 (2006).
56. J. Hlinka, P. Marton, Phenomenological model of a 90° domain wall in BaTiO₃-type ferroelectrics. *Phys. Rev. B* **74**, 104104 (2006).
57. B. Meyer, D. Vanderbilt, Ab initio study of ferroelectric domain walls in PbTiO₃. *Phys. Rev. B* **65**, 104111 (2002).
58. N. F. Quackenbush, H. Paik, M. J. Wahila, S. Sallis, M. E. Holtz, X. Huang, A. Ganose, B. J. Morgan, D. O. Scanlon, Y. Gu, F. Xue, L.-Q. Chen, G. E. Sterbinsky, C. Schlueter, T.-L. Lee, J. C. Woicik, J.-H. Guo, J. D. Brock, D. A. Muller, D. A. Arena, D. G. Schlom, L. F. J. Piper, Stability of the M2 phase of vanadium dioxide induced by coherent epitaxial strain, *Phys. Rev. B* **94**, 085105 (2016).
59. L.-Q. Chen, Phase-field models for microstructure evolution. *Ann. Rev. Mater. Res.* **32**, 113–140 (2002).

Acknowledgments:

Funding: This work was supported by the National Science Foundation under DMREF grant number DMR-1629270, AFOSR grant number FA9550-15-1-0334 and Office of Naval Research N00014-13-1-0183. Transport measurement at the University of Wisconsin-Madison was supported by the US Department of Energy (DOE), Office of Science, Office of Basic Energy Sciences (BES), under award number DE-FG02-06ER46327. The work at Sungkyunkwan University was supported by National Research Foundation of Korea through Basic Research Program (2009-0092809) and KISTI supercomputing center (KSC-2015-C3-067). The work at Penn State is supported by the U.S. Department of Energy, Office of Basic Energy Sciences, Division of Materials Sciences and Engineering under Award FG02-07ER46417 (FX and LQC) and by the NSF MRSEC under Grant No. DMR-1420620 (FX and YS). The research at the University of Nebraska-Lincoln is supported by the National Science Foundation through the Nebraska Materials Science and Engineering Center (MRSEC, Grant No. DMR-1420645).

Author contributions: D.L. and C.B.E. conceived the project. C.B.E., M.S.R., and D.A.T. supervised the experiments. J.L., L.Q.C., and E.Y.T. supervised the theoretical calculations. D.L. and J.P.P. fabricated thin films and performed structural characterization. B.C., T.R.P., E.Y.T., and J.L. performed density functional theory calculations. Y.S., F.X., and L.Q.C. performed phase-field simulations. G.-Y.K., K.S., and S.-Y.C. performed scanning transmission electron microscopy experiments. N.C., T.H.K., J.-H.K., and M.S.R. performed transport measurements. P.J.R. and J.-W.K. performed temperature-dependent X-ray diffraction experiments. J.W.S. and D.A.T. performed Raman spectroscopy experiments. D.L., J.L., L.Q.C., M.S.R., E.Y.T., and C.B.E. prepared the manuscript. C.B.E. directed the overall research.

Competing interests: The authors declare no competing interests.

Data and materials availability: For our DFT calculations, we used VASP, a commercial software package (www.vasp.at/). All data are available in the manuscript or the supplementary materials.

Supplementary Materials:

Materials and Methods

Figs. S1 to S14

Table S1

[References \(39–59\)](#)

[Data](#)

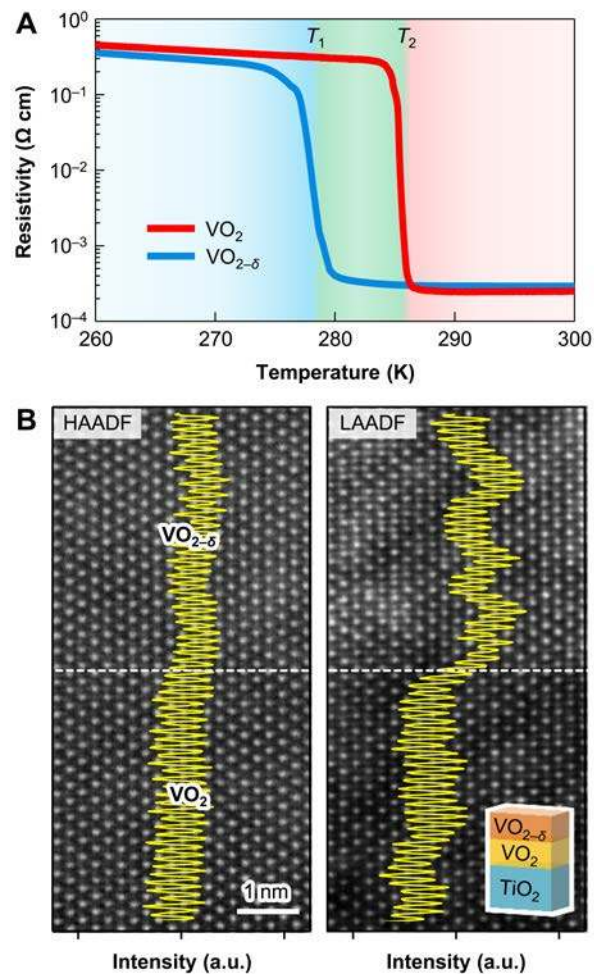


Fig. 1. Design of an artificial $\text{VO}_{2-\delta}/\text{VO}_2$ bilayer. (A) Electrical resistivity measured as a function of temperature of 8-nm-thick epitaxial VO_2 and $\text{VO}_{2-\delta}$ single layer films on (001) TiO_2 substrates. The oxygen vacancy concentration δ is roughly estimated as $\delta \sim 0.01$ (fig. S3). (B) HAADF- and LAADF-STEM images of the $\text{VO}_{2-\delta}/\text{VO}_2$ bilayer (inset) projected along [100]. Yellow lines show the average line profile of the HAADF (left) and LAADF (right) image intensities. White dashed lines represent a nominal interface between VO_2 and $\text{VO}_{2-\delta}$.

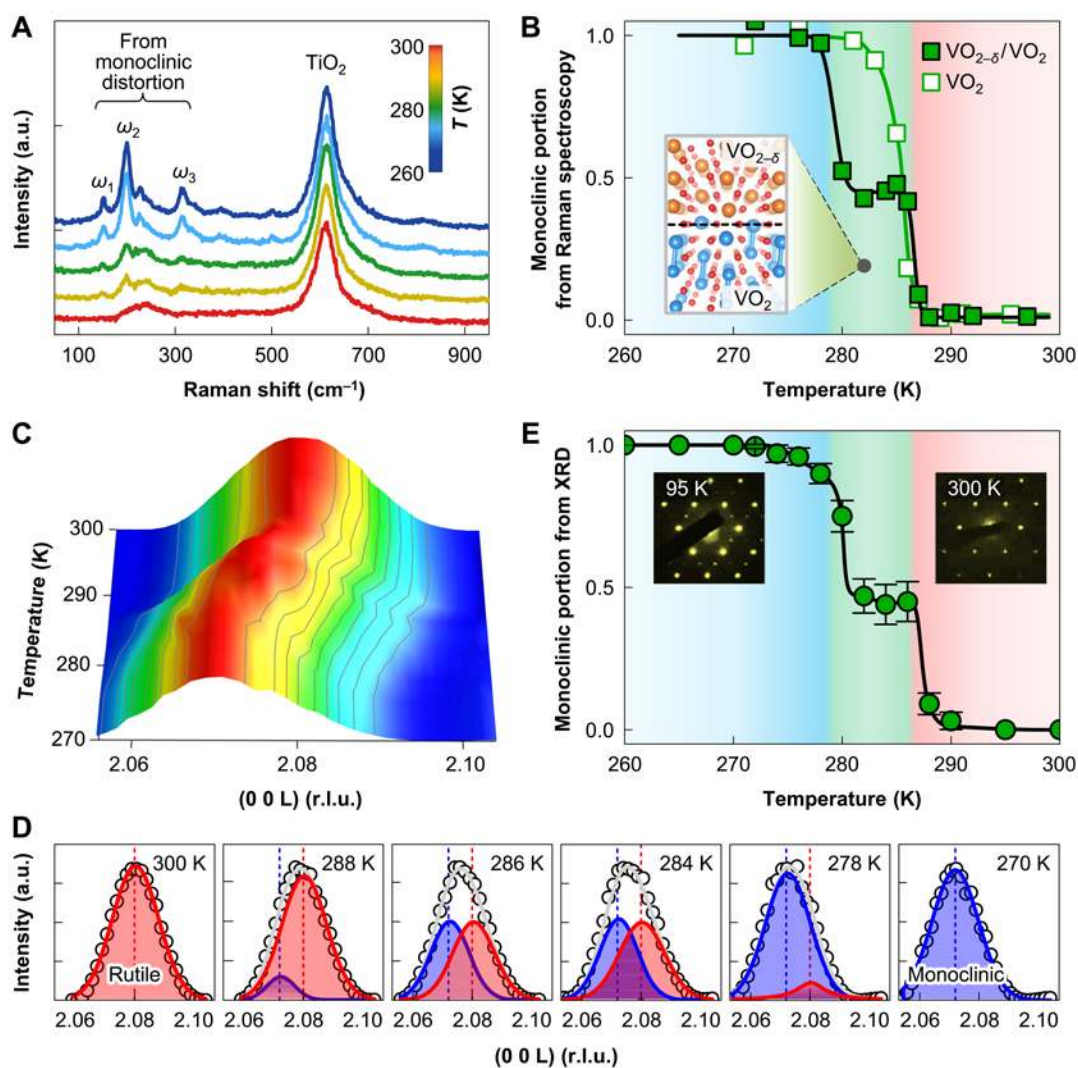


Fig. 2. Structural phase transition in $\text{VO}_{2-\delta}/\text{VO}_2$ bilayer. (A) Raman spectra of $\text{VO}_{2-\delta}$ (8 nm)/ VO_2 (8 nm) bilayer at various temperatures. Raman peaks from the monoclinic distortion are denoted by ω_1 , ω_2 , and ω_3 . (B) Relative monoclinic portion as a function of temperature, estimated from monoclinic Raman intensity in (A). Inset: a schematic for atomic structure of $\text{VO}_{2-\delta}/\text{VO}_2$ bilayer at intermediate temperatures. (C) X-ray diffraction (XRD) (00L) scans of $\text{VO}_{2-\delta}/\text{VO}_2$ bilayer, measured on cooling. (D) Representative XRD peaks at several temperatures. Experimental data (open circles) are fitted using Gaussian curves (solid lines) (E) Relative monoclinic portion as a function of temperature, estimated from XRD peak analysis in (D). Insets show the measured electron diffraction patterns of the bilayer at low and high temperatures.

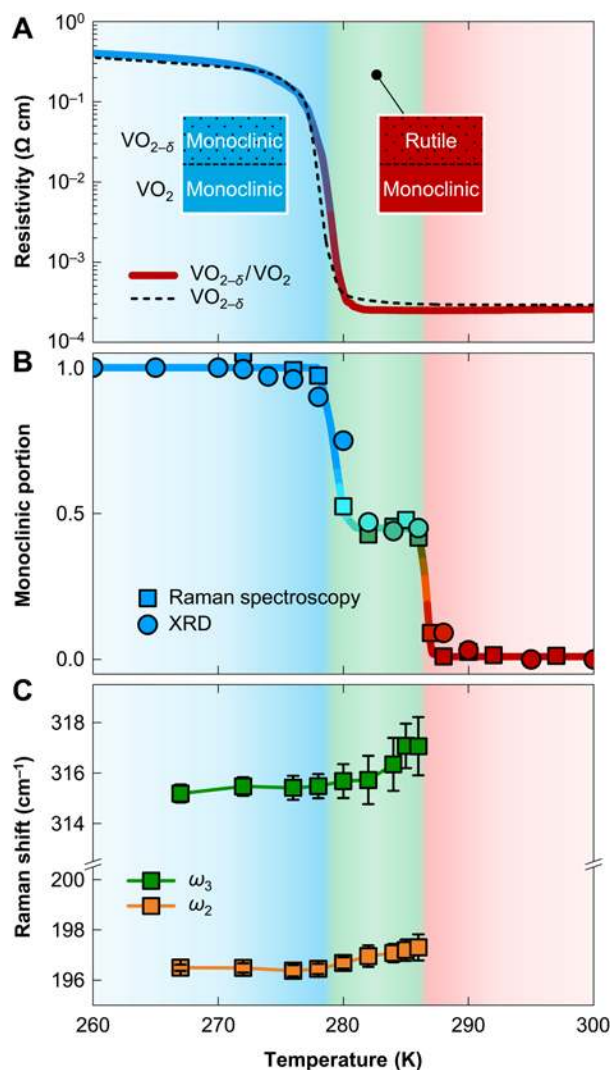


Fig. 3. Isostructural metal-insulator transition in $\text{VO}_{2-\delta}/\text{VO}_2$ bilayer. (A) Electrical resistivity vs. temperature of $\text{VO}_{2-\delta}$ (8 nm)/ VO_2 (8 nm) bilayer (solid line) and 8-nm-thick $\text{VO}_{2-\delta}$ single layer (black dashed line), measured on cooling. Metallic and insulating phases are represented by red and blue colors, respectively. (B) Monoclinic portion (from Figs. 2, B and E) as a function of temperature. (C) Temperature dependence of monoclinic Raman shift, i.e., ω_2 and ω_3 in Fig. 2A.

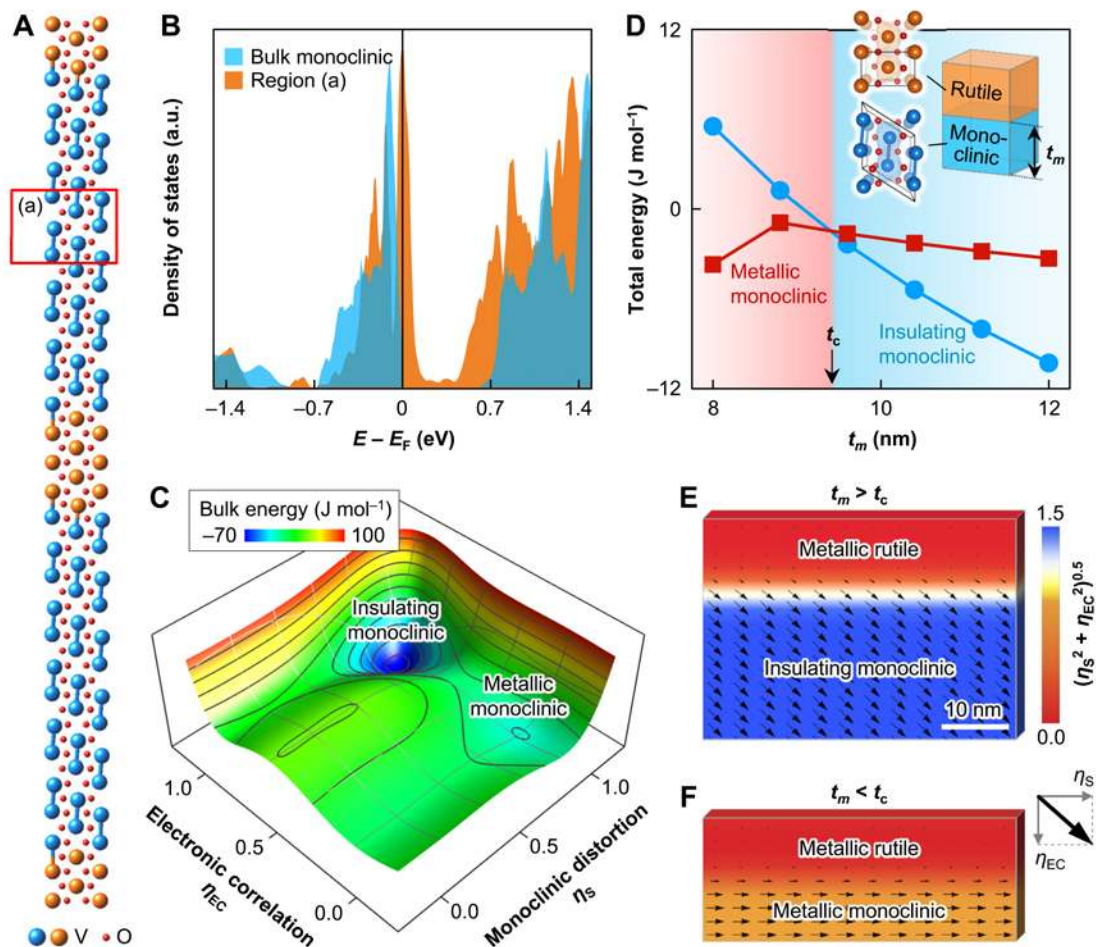


Fig. 4. Theoretical modeling of the metallic monoclinic VO_2 phase. (A) The rutile/monoclinic heterostructure used in the DFT calculation (28). V atoms are shown in two colors, i.e., orange for rutile VO_2 and blue for monoclinic VO_2 . (B) The calculated density of states of the local monoclinic region [denoted by (a) in A] in the rutile/monoclinic heterostructure shows a metallic nature, distinct from the insulating nature of the bulk monoclinic VO_2 (blue colored). (C) Free energy landscape of bulk VO_2 at 287 K, just below the transition temperature. (D) Total energies as a function of t_m in the rutile/monoclinic heterostructure. t_c is estimated to be ~ 9.4 nm. (E and F) Stable states of the rutile/monoclinic heterostructure for $t_m > t_c$ (E) and $t_m < t_c$ (F). The arrows represent the two-component order parameter (η_s, η_{EC}) , and the color represents the norm $(\eta_s^2 + \eta_{EC}^2)^{0.5}$.



Supplementary Materials for **Isostructural metal-insulator transition in VO₂**

D. Lee, B. Chung, Y. Shi, G.-Y. Kim, N. Campbell, F. Xue, K. Song, S.-Y. Choi, J. P. Podkaminer, T. H. Kim, P. J. Ryan, J.-W. Kim, T. R. Paudel, J.-H. Kang, J. W. Spinuzzi, D. A. Tenne, E. Y. Tsymbal, M. S. Rzchowski, L. Q. Chen, J. Lee*, C. B. Eom*

correspondence to: eom@engr.wisc.edu (C.B.E.), jclee@skku.edu (J.L.)

This PDF file includes:

Materials and Methods
Figs. S1 to S14
Table S1
Full Reference List

Materials and Methods

Thin film fabrication

VO₂ epitaxial thin films were grown on rutile TiO₂ (001) substrate using the pulsed laser deposition (PLD) method. A KrF excimer laser (248 nm) beam was focused on the vanadium metal target to an energy density of $\sim 2.0 \text{ J cm}^{-2}$ and pulsed at 10 Hz. VO₂ films were grown at a substrate temperature of 300 °C and oxygen partial pressures (P_{O_2}) ranging from 12 to 24 mTorr. The stoichiometric VO₂ and slightly oxygen-deficient VO_{2- δ} films were deposited at P_{O_2} of 21 and 18 mTorr, respectively. [We roughly estimated the δ value to be ~ 0.01 (Fig. S3).] The crystal structure of the films was determined using a high-resolution four-circle XRD machine (Bruker D8 advance). Figures S2A–C represent the results of XRD 2θ - ω scans, rocking curve, and reciprocal space mapping (RSM), respectively, for our VO₂ films. The full width at half maximum (FWHM) of rocking curve was measured as small as 0.017° (Fig. S2B), indicating the excellent crystalline quality of VO_{2- δ} /VO₂ bilayer. From the RSM data (Fig. S2C), we confirmed that the VO_{2- δ} /VO₂ bilayer is fully coherent with the TiO₂ substrate without any strain relaxation. Film surfaces were imaged by atomic force microscopy (AFM; Fig. S2D).

We roughly estimated the concentration of oxygen vacancies in the films from the measured unit-cell volume. According to the empirical model, the unit-cell volume V can be expressed as follows (39):

$$r_M = A \cdot V^{1/3} - B \quad (\text{Eq. S1})$$

where r_M is the ionic radius of the cation, V is the unit cell volume, and A and B are constants. From the relationship between r_M and V in rutile oxides, we determined A and B to be 0.4555 and 1.2001, respectively (Fig. S3A). By assuming oxygen-deficient VO_{2- δ} for simplicity, we can define the effective cation radius as (40):

$$r_M = (1 - 2\delta) \cdot r_{V^{4+}} + (2\delta) \cdot r_{V^{3+}} = 0.58 + 0.12\delta \quad (\text{Eq. S2})$$

where $r_{V^{4+}}$ and $r_{V^{3+}}$ are the ionic radii of V⁴⁺ and V³⁺, respectively. The values for these radii are all available from the work of Shannon (41). Then, we determined the δ values (i.e., the concentration of oxygen vacancies) from the measured unit-cell volume as follows (Fig S3B):

$$\delta = \frac{0.4555 \times (V_{\text{stoichiometric}} + \Delta V)^{1/3} - 1.78001}{0.12} \quad (\text{Eq. S3})$$

where $V_{\text{stoichiometric}}$ and $V_{\text{stoichiometric}} + \Delta V$ are the unit cell volume of stoichiometric VO₂ and oxygen deficient VO_{2- δ} , respectively. As shown in Fig. S3B, the δ value was roughly estimated as ~ 0.01 for the VO_{2- δ} film grown at $P_{\text{O}_2} = 18$ mTorr. Note that since the precise determination of the oxygen-vacancy concentration is very elusive, this estimation method should be meaningful only for the relative comparison.

The VO_{2- δ} /VO₂ bilayer was prepared, by first growing the VO₂ layer at $P_{\text{O}_2} = 21$ mTorr and then growing the VO_{2- δ} layer at $P_{\text{O}_2} = 18$ mTorr (Fig. S1). For confirming that the P_{O_2} variation after growth doesn't affect the physical properties of the already-grown VO₂ films, we prepared two samples (Fig. S4): Whereas one sample was grown and cooled at $P_{\text{O}_2} = 21$ mTorr, the other was grown at $P_{\text{O}_2} = 21$ mTorr, then annealed for 10 minutes at a reduced $P_{\text{O}_2} = 17$ mTorr, and cooled at $P_{\text{O}_2} = 17$ mTorr. Figure S4 exhibits the XRD and transport data for those samples, showing negligible change in sample properties even after the additional annealing at the reduced

P_{O_2} . This indicates that while the P_{O_2} variation during growth affects the oxygen stoichiometry and the resulting metal-insulator transition of VO_2 films, the P_{O_2} variation after growth doesn't affect those much, consistent with other previous works (29).

To check if the sequence of $VO_{2-\delta}$ and VO_2 layer in the bilayer affects the phase transitions, we grew two different bilayers, i.e., $VO_{2-\delta}/VO_2$ and $VO_2/VO_{2-\delta}$ bilayers, on TiO_2 (001) substrate. The $VO_2/VO_{2-\delta}$ bilayer was prepared, by first growing the $VO_{2-\delta}$ layer at $P_{O_2} = 18$ mTorr and then growing the VO_2 layer at $P_{O_2} = 21$ mTorr. As shown in Fig. S7A, the sequence of $VO_{2-\delta}$ and VO_2 layer in the bilayer didn't induce any change in phase transitions. The metal-insulator transitions of both the $VO_{2-\delta}/VO_2$ and $VO_2/VO_{2-\delta}$ bilayers follow that of the $VO_{2-\delta}$ single layer.

Scanning transmission electron microscopy (STEM) and EELS

For electron microscopic analysis, we prepared the thin, electron-transparent sample using the conventional method (mechanical thinning to ~ 10 μm or less; and ion beam milling to electron transparency at an acceleration voltage of 0.5–3.5 kV using an Ar ion beam). The atomic structures were observed using a STEM (JEOL JEM-2100F, JEOL Ltd., Japan) with an aberration corrector (CEOS GmbH, Heidelberg, Germany); and its probe diameter and convergence angle of the beam were ~ 0.9 Å and ~ 24 mrad under the acceleration voltage of 200 kV, respectively. The collection semiangles of the detectors for high angle annular dark field (HAADF) and low angle annular dark field (LAADF) imaging were greater than 80–200 and 30–60 mrad, respectively. The obtained STEM images were local Wiener filtered to reduce background noise (HREM Research Inc., Japan).

In contrast to the HAADF, so called Z-contrast, which provides the atomic weight, LAADF can provide the qualitative information of the atomic dechanneling mainly caused by the strain or the vacancies due to the low-order diffractions of electrons, close to the on-axis (29, 42, 43). As shown in Fig. S5, the HAADF and LAADF contrasts are profiled for better visualization, wherein the stronger LAADF contrast from the upper half indicates the existence of oxygen vacancies. LAADF image confirms that our film consists of VO_2 and $VO_{2-\delta}$ layers.

Energy loss spectra were obtained at 200 kV using an electron energy loss spectrometer (EELS; Quantum GIF, Gatan, United States) with an energy resolution of 0.8 eV (Fig. S6). Theoretical calculation of V- $L_{2,3}$ and O-K edge EELS were performed by using the DFT calculation, CASTEP embedded in Materials Studio (Biovia, United States). For the calculation, a $3 \times 3 \times 3$ supercell of rutile VO_2 was used; the interactions among the electrons were calculated by using the core-hole method; and the electronic interactions were treated as the local density approximation.

Suppression of the first peak in V- $L_{2,3}$ and the second peak in O-K is related with the less electron density in p -V and s -O orbitals caused by the oxygen vacancies. The measured EELS data for the VO_2 and $VO_{2-\delta}$ layers were consistent with the calculated results for VO_2 and $VO_{1.98}$ (Fig. S6).

Electrical transport measurements

We monitored the metal-insulator transition in VO_2 films by measuring their electrical resistivity as a function of temperature. Electrical resistivity was measured using a four-contact

van der Pauw technique. For the transport measurements, we tried both indium and aluminum metal contacts, and found little change in the data. We observed that the metal-insulator transition (e.g., the transition temperature) of VO_{2-δ}/VO₂ bilayer was almost identical to that of VO_{2-δ} single layer (Fig. 3A). If the VO₂ and VO_{2-δ} layers in the bilayer are independent with each other without any interaction, there should be clear two-step signature in the metal-insulator transition, as shown in Fig. S8A. To confirm this, we intentionally suppressed the interfacial effect by inserting an ultrathin (~2 nm) TiO₂ layer between VO_{2-δ} and VO₂. The VO_{2-δ}/TiO₂/VO₂ trilayer showed a clear two-step metal-insulator transition (Fig. S8B), which verifies the interfacial effect as the intrinsic origin of the collective, single-step metal-insulator transition in the VO_{2-δ}/VO₂ bilayer.

Hall measurements were conducted sourcing a DC current and sweeping the magnetic field over a range of -7 T to 7 T. All Hall data were linear with respect to magnetic field. Consequently, we fit to a single-band model, using $n_{3D} = \frac{I}{\frac{dV_H}{dB} \cdot t \cdot q}$ to extract the carrier density (Fig. S7B). In

the previous expression, I is the DC current sourced, V_H the Hall voltage, t the thin-film thickness, and q the electron charge.

Raman spectroscopy

Raman spectra of VO₂ thin films grown on TiO₂ (001) substrates have been measured in backscattering geometry normal to the film surface using a Jobin Yvon T64000 triple spectrometer equipped with a liquid nitrogen cooled multichannel charge coupled device detector. We tried several excitation wavelengths, visible (442 and 488 nm), and UV (325 and 363.8 nm). It was found that with visible excitation the spectra are dominated by the substrate signal. 363.8-nm excitation was chosen as it resulted in a stronger signal from VO₂ films. Spectra were measured in the temperature range 250–300 K using a variable temperature closed cycle helium cryostat. The high-temperature metallic phase of bulk VO₂ has a tetragonal rutile structure with space group D_{4h}^{14} ($P4_2/mnm$) and four Raman-active phonons (31). In metallic phase, the phonon peaks are very broad and weak; they are hardly observable even in the bulk (31, 44). In our thin film samples, the spectra above the transition temperature contain the TiO₂ substrate features only. The low-temperature phase has a monoclinically distorted structure with space group C_{2h}^5 ($P2_1/c$). The unit cell doubles in size in the monoclinic phase, which has 18 Raman-active phonons (9A_g and 9B_g modes). In the low-temperature spectra, seven A_g modes can be distinguished at 151, 225, 196, 316, 393, 457, and 499 cm⁻¹ (two more A_g modes that should appear around 595 and 618 cm⁻¹ are masked by strong peak of the TiO₂ substrate at 612 cm⁻¹). Also, three B_g modes can be seen at 335, 437, and 812 cm⁻¹; the others being either too weak or overlapped by the substrate features.

We obtained the temperature dependence of relative Raman intensity of two most intensive VO₂ peaks (i.e., ω_2 and ω_3 near 196 and 316 cm⁻¹), which originate from the monoclinic distortion in VO₂ (Fig. 2B). The integrated intensities of these peaks were normalized by the integrated intensity of the 612 cm⁻¹ peak of TiO₂ substrate. Initially at high temperatures, VO₂ is in the tetragonal rutile phase, and the intensity of the monoclinic VO₂ peaks is essentially zero. With decreasing temperatures, the Raman peaks of monoclinic VO₂ appeared suddenly during the rutile-to-monoclinic structural phase transition (Figs. 2A and B). Our Raman spectroscopy

measurements showed that the $\text{VO}_{2-\delta}/\text{VO}_2$ bilayer has a two-step structural phase transition (Fig. 2B), whereas the VO_2 single layer has a single-step structural phase transition (Fig. S9).

X-ray diffraction measurement

We monitored the rutile-to-monoclinic structural phase transition by conducting X-ray diffraction (XRD) (00L) scans on cooling. Before the measurement, sample was aligned using the (002) reflection of the TiO_2 substrate. Due to the increased out-of-plane lattice during monoclinic distortion, the center L (Reciprocal Lattice Units-RLU) position of the XRD peaks is shifted from ~ 2.080 (for high-temperature rutile) to ~ 2.072 (for low-temperature monoclinic). Based on this, we fit the measured XRD peaks using two Gaussian curves (shown as red and blue curves in Fig. 2D) with the L values of 2.080 ± 0.0005 RLU (for rutile) and 2.072 ± 0.0005 RLU (for monoclinic). We estimated the relative monoclinic portion as $A_{\text{Mc}}/(A_{\text{Mc}} + A_{\text{R}})$, where A_{R} and A_{Mc} correspond to the area under the two fitted Gaussian curves. In Figs. 2C and D, we normalized the maximum peak intensity with the value at 300 K.

Density functional calculation

The calculations were performed using density functional theory (DFT) as implemented in Vienna *ab initio* simulation package (VASP) (45, 46). Non-spin-polarized calculation and Hubbard U correction were used since all spin-polarized calculations employing local density approximation (LDA (+ U)), Perdew-Burke-Ernzerhof (PBE (+ U)), or Heyd-Scuseria-Ernzerhof (HSE) hybrid functional method did not properly predict an insulating monoclinic ground state (33). The projected augmented wave (PAW) method was used to approximate the electron-ion potential (47). To treat exchange and correlation effects, we used LDA (48) within the semi-empirical + Hubbard U (LDA + U) approach (49, 50) and a rotationally invariant formalism (51), for a better description of the localized transition metal d electrons. Here we used $U_d = 3.8$ eV and $J_d = 0.8$ eV for the rutile structure's V-3d orbitals and $U_d = 4.63$ eV and $J_d = 0.7$ eV for the monoclinic structure's V-3d orbitals to produce the correct ground state phase. In the middle of the Coulomb correction, fine tuning of U values was made to fit the band gap of the monoclinic phase and the gap between O2p and V3d states of the rutile phase. $3s^2 3p^6 3d^3 4s^2$ and $2s^2 2p^4$ valence electron configurations were used for vanadium and oxygen, respectively. For the relaxation of internal co-ordinate, we used ionic convergence criterion of $|0.01|$ eV/Å with a plane-wave cutoff energy of 500 eV (for rutile and monoclinic bulks, and rutile/monoclinic superlattice). Γ -centered k -mesh of $6 \times 3 \times 1$ was employed in tetrahedron method with Blöchl corrections.

For heterostructure, $1 \times 2 \times 10$ unit cell [(rutile) $_5$ /(monoclinic) $_5$] supercell was used. To describe relaxed and abrupt (001)_{Rutile} interfaces in the heterostructure, seven and eight VO_2 layers of rutile and monoclinic phases near the abrupt interface, respectively, were fixed. The rutile and monoclinic unit cells include 2 and 4 VO_2 layers, respectively. The in-plane lattice parameter was fixed, while the out-of-plane lattice parameter and the internal co-ordinates were relaxed. The in-plane lattice parameter, $a = b = 4.5446$ Å, was used, and the out-of-plane lattice parameters, 2.8512 Å and 5.5300 Å, were used for rutile and monoclinic regions, respectively. After the relaxation of superlattices, three layers of the rutile phase near the relaxed interface showed the dimerization of V-V-V, resembling a monoclinic phase and out-of-plane lattice parameter was 41.707 Å. Then, 6-unit-cell-thick layer in the superlattice was treated as the monoclinic phase (Fig. 4A).

Figure S10 shows a layer-resolved profile of the density of states (DOS) and V-V-V bond angle in the superlattice. Within the cell size used in our calculations, the whole monoclinic region exhibited a metallic characteristic, i.e., non-zero DOS at Fermi energy (E_F). To check possible contribution from structural relaxation (i.e., variation of monoclinic distortion and the V-V-V bond angle) at interfaces, we considered the abrupt interface (i.e., lower interface in Fig. S10A), as well as the relaxed broad interface (i.e., upper interface in Fig. S10A). We found that the metallization of monoclinic VO₂ occurred regardless of the types of interfaces. Furthermore, we calculated the density of states by capturing local monoclinic structures within the monoclinic region of the superlattice (Fig. S11), and found that the local structural modification itself did not cause any metallicity in monoclinic VO₂. This result excludes main contribution of the interfacial structural relaxation and indicates a purely electronic origin behind the metallization of monoclinic VO₂.

The relaxed and abrupt (001)_{Rutile} interface energies ($E_{i,rel}$, $E_{i,abr}$) were calculated by subtracting the bulk energies of monoclinic and rutile phases from the total energy of the monoclinic (n)/rutile (m) (001)_{Rutile} superlattices (Fig. S10A):

$$E_{i,rel} = E_{HS} - nE_{MC} - mE_R - E_{i,abr} \quad (\text{Eq. S4})$$

$$E_{i,abr} = (E_{HS,fix} - nE_{MC} - mE_R) / 2A \quad (\text{Eq. S5})$$

Here, n and m are the number of unit cells, E_{MC} and E_R are the bulk energies of monoclinic and rutile phases per unit cell, respectively. E_{HS} is the total energy of the superlattice, $E_{HS,fix}$ is the total energy of the superlattice before relaxation, A is the in-plane lateral area of a unit cell, and a factor of two takes into account the presence of two interfaces in the superlattice. The calculated interface energy $E_{i,rel}$ was found to be small $E_{i,rel} = 69 \text{ mJ m}^{-2}$, comparable to accuracy of our calculations. This value is much smaller than typical interfacial energies $\sim 1 \text{ J m}^{-2}$ in metal/insulator interfaces (52, 53).

Figure S12 shows the calculated density of states of hole-doped and electron-doped monoclinic VO₂. We found that increasing hole concentration causes a significant band gap narrowing, whereas the electron doping doesn't much affect the gap. The gap decreases with the increasing hole doping (i.e., lower d band occupation) and finally collapses at high hole doping, which can be interpreted as the decrease in the strength of electron correlation (22). Notably, the density of states of the hole-doped monoclinic VO₂ looks similar to that of the metallic monoclinic region in the rutile/monoclinic superlattice (Fig. 4B).

Landau theory and phase-field simulation

The metal-insulator and structural transition in VO₂ can be characterized by an electron-correlation order parameter η_{EC} and a structural order parameter η_S , respectively. η_{EC} denotes the electron spin density correlation between the electrons of two adjacent V atoms, and η_S characterizes the dimerization of the V atoms. Nonzero η_{EC} indicates the formation of the dynamical singlet and consequently the spin gap (15), corresponding to the insulating phase, while $\eta_{EC} = 0$ refers to the metallic phase. The bulk molar Landau potential can be written as

$$f_b = \frac{1}{2}a_1 \frac{T-T_{EC}}{T_{EC}}\eta_{EC}^2 + \frac{1}{4}b_1\eta_{EC}^4 + \frac{1}{6}c_1\eta_{EC}^6 + \frac{1}{2}a_2 \frac{T-T_S}{T_S}\eta_S^2 + \frac{1}{4}b_2\eta_S^4 + \frac{1}{6}c_2\eta_S^6 - g_1\eta_{EC}\eta_S - \frac{1}{2}g_2\eta_{EC}^2\eta_S^2, \quad (\text{Eq. S6})$$

where a_1 , b_1 , c_1 , a_2 , b_2 , c_2 , g_1 , and g_2 are coefficients of the Landau polynomial, and are fitted based on the transition temperature and the entropy of transformation measured in this work and other experiments (54). The values of all the coefficients are listed in Table S1. Note that the experimental data are not enough to uniquely determine all the coefficients. However, the analysis and phase-field simulations are not very sensitive to the values of all the individual coefficients as long as they reproduce the critical features such as transition temperatures and relative stabilities of different phases, and thus the physics presented in the main text is insensitive to the choice of some of the coefficients.

In the phase-field simulations, the gradient energy is taken into account

$$F_{grad} = \int d^3r \left[\frac{1}{2}k_1(\nabla\eta_{EC})^2 + \frac{1}{2}k_2(\nabla\eta_S)^2 \right], \quad (\text{Eq. S7})$$

The gradient energy coefficients k_1 and k_2 are positive and fitted to the interfacial energy of 50 mJ m^{-2} , which is arbitrarily chosen between an experimental estimation of 25 mJ m^{-2} (55) and a calculated upper bound of 69 mJ m^{-2} from our DFT simulation. Although the experiments cannot distinguish the contribution from the variation of η_{EC} and that of η_S , we can make a reasonable assumption that $k_1 > k_2$ since the bulk free energy of the electronic order parameter is of the same order with that of the structural order parameter in Eq. S6 based on the coefficients in Table S1 and the interfacial energy of a metal-insulator interface is typically larger than that of an interface separating two pure structural domains (the metal-insulator interfacial energy has the typical value $\sim 1 \text{ J m}^{-2}$ (52, 53), whereas the interfacial energy of two pure structural domains is within the range $0.01\text{--}0.2 \text{ J m}^{-2}$ (56, 57)). The values of the gradient energy coefficients are listed in Table S1.

The energy landscapes of the bulk Landau potential at different temperatures are shown in Fig. S13. Above the transition temperature T_{PT} , the rutile phase ($\eta_{EC} = 0$, $\eta_S = 0$) appears as the global minimum, i.e., the stable phase. Below the transition temperature, besides the insulating monoclinic stable phase ($\eta_{EC} = 1$, $\eta_S = 1$), we can also see a local minimum with order parameters $\eta_{EC} = 0$ and $\eta_S = 1$, which is identified as the metastable metallic monoclinic phase. The metastable metallic monoclinic phase disappears below $T_m \sim T_{PT} - 12 \text{ K}$.

For $\text{VO}_{2-\delta}$, we assume that the Curie temperatures T_{EC} and T_S in Eq. S6 are decreased by the same amount, i.e., 10 K . The decrease may be caused by the off-stoichiometry and/or the tensile strain from the bottom VO_2 layer, since the transition temperature in VO_2 is decreased under a tensile strain (58). Note that for the individual $\text{VO}_{2-\delta}$ layer, although the transition temperature is decreased, the electronic transition and structural transition are always coupled. However, for the $\text{VO}_{2-\delta}/\text{VO}_2$ bilayer geometry, when the temperature T_m is between the transition temperature of VO_2 and $\text{VO}_{2-\delta}$ layers, the situation is different. At T_m , the $\text{VO}_{2-\delta}$ layer is in the metallic rutile phase. For the VO_2 layer, the possible phases can be the insulating monoclinic or metallic monoclinic phases. Across the metallic rutile/insulating monoclinic interface, both the order parameters η_{EC} and η_S vary spatially, while across the metallic rutile/metallic monoclinic interface, only η_S varies, which results in smaller interfacial energy in the latter. This conclusion is insensitive to the specific value of k_1 and k_2 under the condition that both k_1 and k_2 are positive,

which is almost always true. Denoting the interfacial energy difference between the two cases as Δf_{int} , and the bulk molar free energy difference between insulating monoclinic phase and metallic monoclinic phase as Δf_b (Figs. S14A and B), one can calculate a critical thickness (V_m is the molar volume of the rutile phase)

$$t_c = \frac{\Delta f_{\text{int}} V_m}{\Delta f_b}, \quad (\text{Eq. S8})$$

below which the total free energy of the metallic monoclinic/rutile geometry will be lower than that of the insulating monoclinic/rutile geometry, resulting in a stable metallic monoclinic phase in the VO₂ layer. Therefore, although the metallic monoclinic phase has a larger bulk free energy than the insulating monoclinic phase, it can be stabilized below a critical thickness due to the smaller interfacial energy. Note that the specific value of t_c depends on the choice of k_1 and k_2 .

Next we employ phase-field simulations to confirm the above hypothesis (59). The order parameters are evolved by solving the time-dependent Ginzburg-Landau (TDGL) equations

$$\frac{\partial \eta_{EC}}{\partial t} = L_{EC} \frac{\delta F}{\delta \eta_{EC}} \quad \& \quad \frac{\partial \eta_s}{\partial t} = L_s \frac{\delta F}{\delta \eta_s}, \quad (\text{Eqs. S9 and 10})$$

where L_{EC} and L_s are the kinetic coefficients related to the domain wall mobility, and F is given by $F = \int f_b dn + F_{\text{grad}}$. In Fig. S14C, we present the phase-field simulations of the stable phases of the bilayer system at different temperatures. As can be seen, the metallic monoclinic phase is stabilized at $T = 283$ K in the VO₂ layer due to the interaction between the two layers.

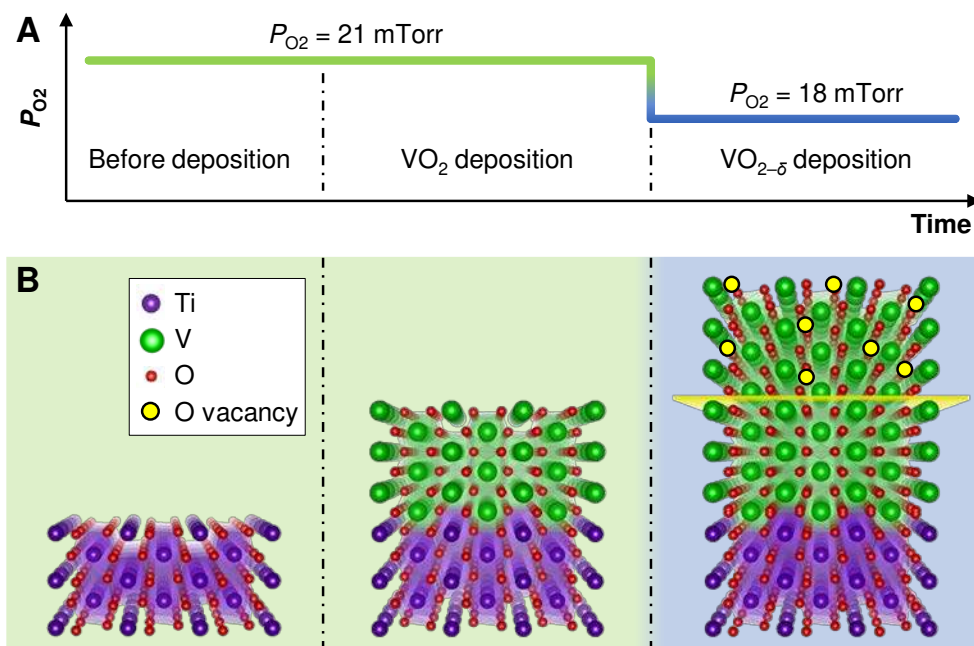


Fig. S1. Growth of $\text{VO}_{2-\delta}/\text{VO}_2$ bilayer. (A and B) By changing the oxygen partial pressure (P_{O_2}) during film growth [as shown in (A)], we can prepare the $\text{VO}_{2-\delta}/\text{VO}_2$ bilayer nanostructure [as shown in (B)], which has two distinct transition temperatures in its upper (i.e., $\text{VO}_{2-\delta}$) and lower (VO_2) layers.

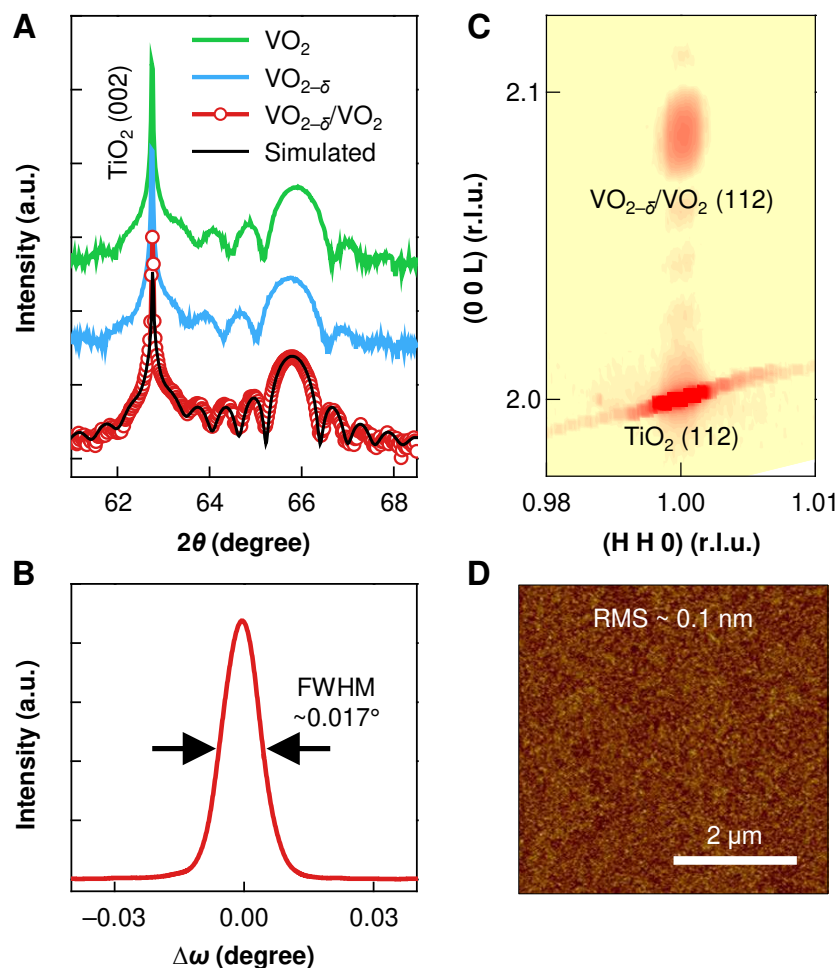


Fig. S2. Structural characterization of $\text{VO}_{2-\delta}/\text{VO}_2$ bilayer. (A) X-ray diffraction (XRD) 2θ - ω scans of VO_2 single layer, $\text{VO}_{2-\delta}$ single layer, and $\text{VO}_{2-\delta}/\text{VO}_2$ bilayer. We also represent the simulated result for $\text{VO}_{2-\delta}/\text{VO}_2$ bilayer, which is well matched with the experimental data. (B) Rocking curve of the XRD (002) reflection for $\text{VO}_{2-\delta}/\text{VO}_2$ bilayer. (C) XRD reciprocal space map around the (112) reflections of TiO_2 substrate and $\text{VO}_{2-\delta}/\text{VO}_2$ bilayer. (D) Atomic force microscopy image of $\text{VO}_{2-\delta}/\text{VO}_2$ bilayer, showing smooth surface of the film.

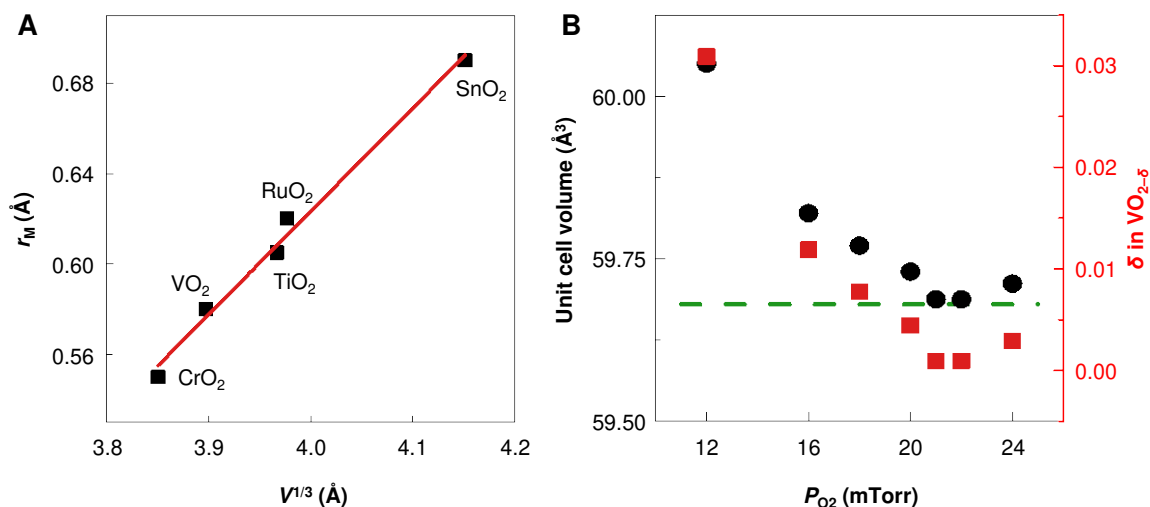


Fig. S3. Rough estimation of oxygen stoichiometry. (A) Linear relationship between r_M and $V^{1/3}$ in rutile oxides. (B) The measured unit cell volume and the estimated oxygen-vacancy concentration δ in the VO_2 films, as a function of oxygen partial pressure (P_{O_2}) used during film growth.

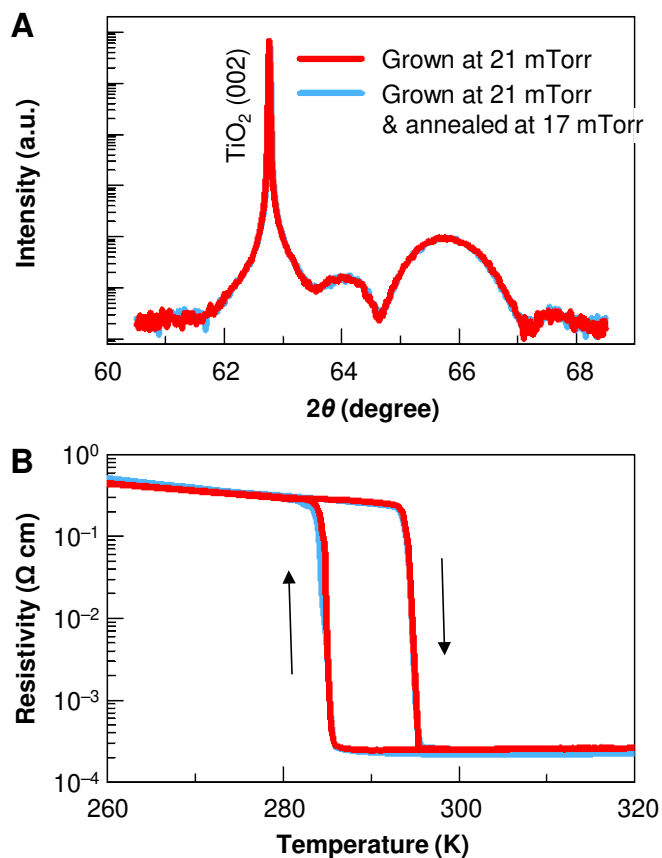


Fig. S4. No effect of the “after-growth” change of P_{O_2} . (A) X-ray diffraction (XRD) 2θ - ω scans of two VO_2 samples. Red line is for the sample that was grown and cooled at $P_{\text{O}_2} = 21$ mTorr. Blue line is for the sample that was grown at $P_{\text{O}_2} = 21$ mTorr, annealed for 10 minutes at a reduced $P_{\text{O}_2} = 17$ mTorr, and cooled at $P_{\text{O}_2} = 17$ mTorr. (B) Electrical resistivity as a function of temperature for two VO_2 samples in (A).

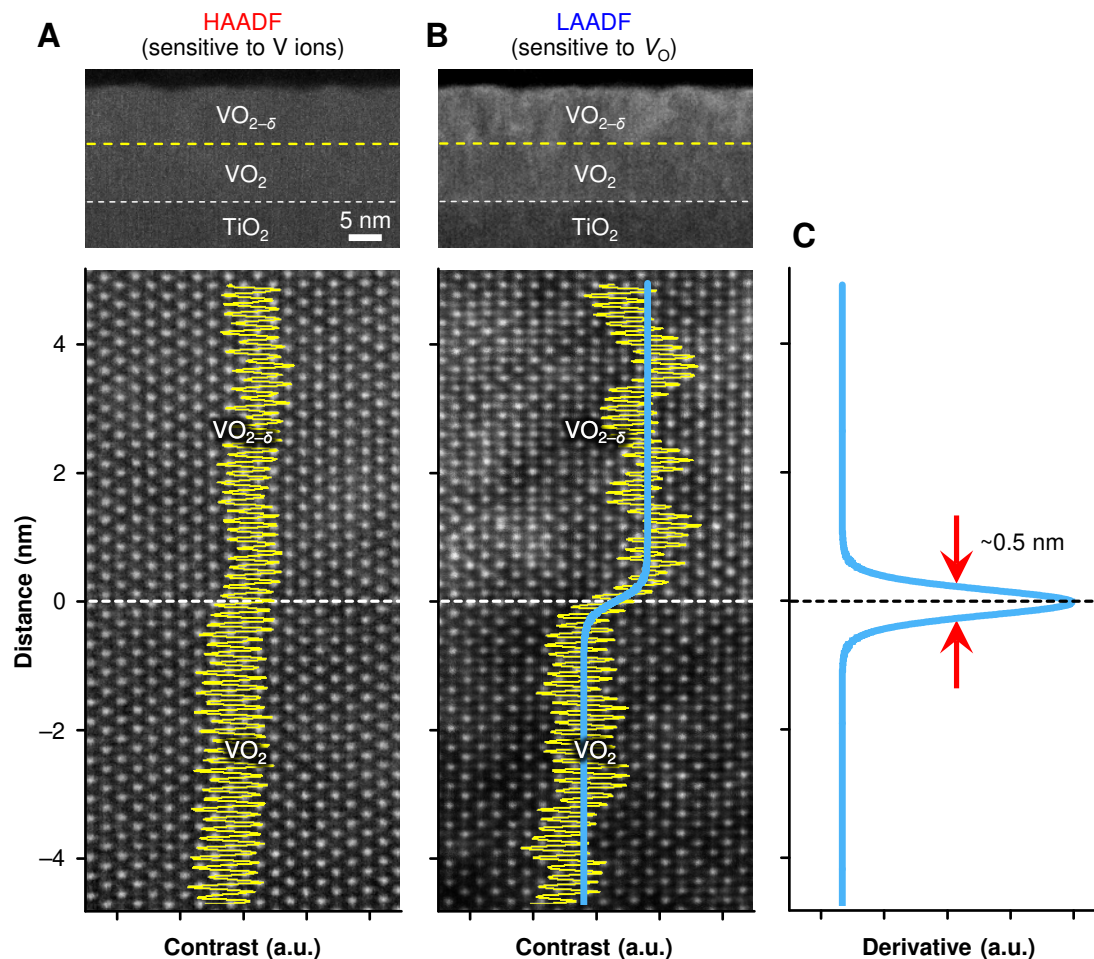


Fig. S5. Nanoengineered oxygen stoichiometry. (A and B) High angle annular dark field (HAADF) (A) and low angle annular dark field (LAADF) (B) images, which are sensitive to V atomic lattice and oxygen vacancy, respectively. Yellow lines indicate measured contrast profile through atomic columns and white dashed lines represent a nominal interface between VO_2 and $\text{VO}_{2-\delta}$. (C) Derivative of the fitted line (solid blue) for the LAADF contrast profile in B.

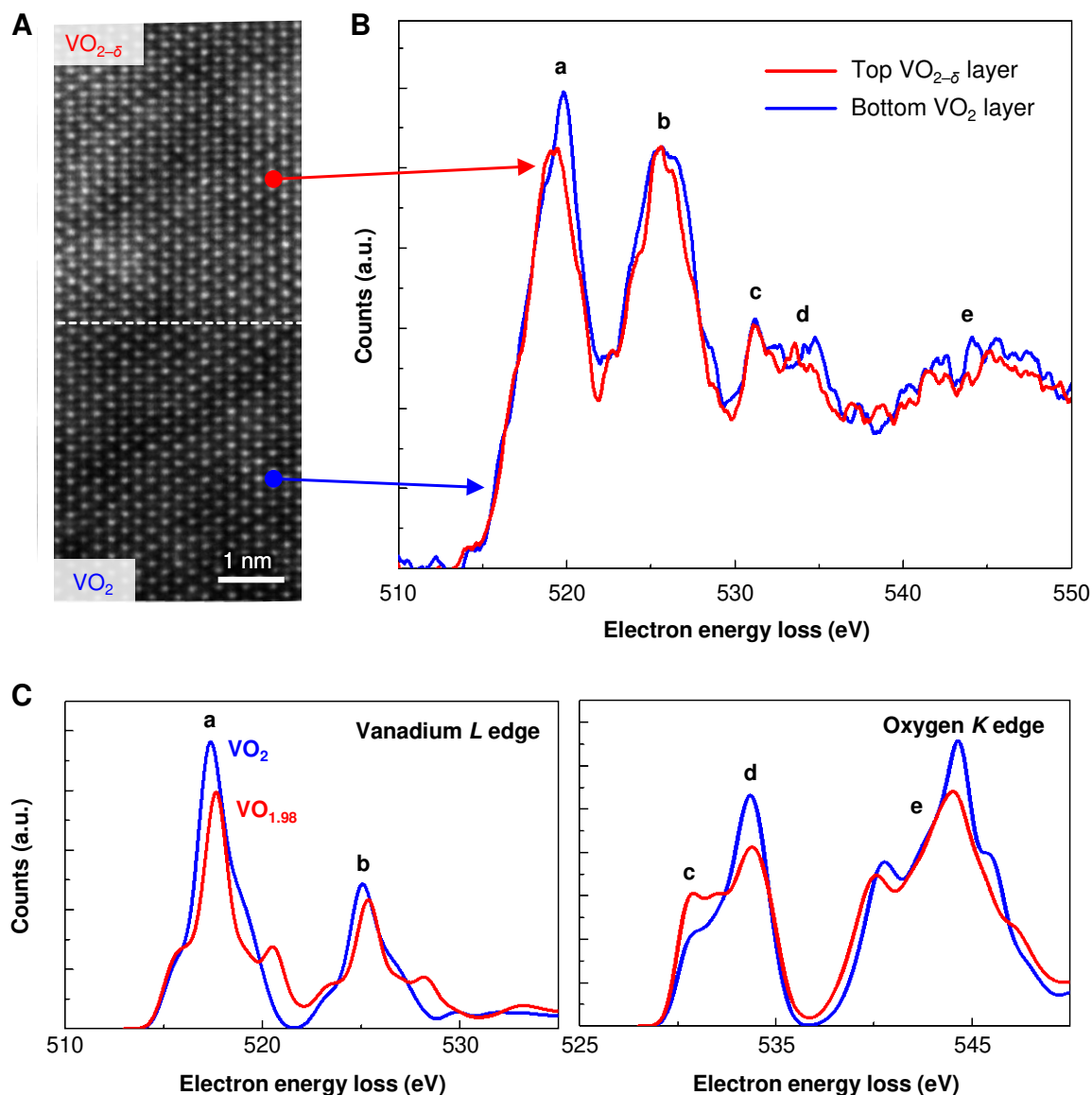


Fig. S6. EELS analysis of oxygen stoichiometry. (A) LAADF-STEM image of $\text{VO}_{2-\delta}/\text{VO}_2$ bilayer. (B) Measured V- $L_{2,3}$ (a and b peaks) and O- K edges (c, d, and e peaks) for the top $\text{VO}_{2-\delta}$ (red) and bottom VO_2 (blue) layers of $\text{VO}_{2-\delta}/\text{VO}_2$ bilayer. (C) Calculated EELS data for the vanadium $L_{2,3}$ (left) and oxygen K (right) edges. Blue and red lines correspond to VO_2 and $\text{VO}_{1.98}$, respectively.

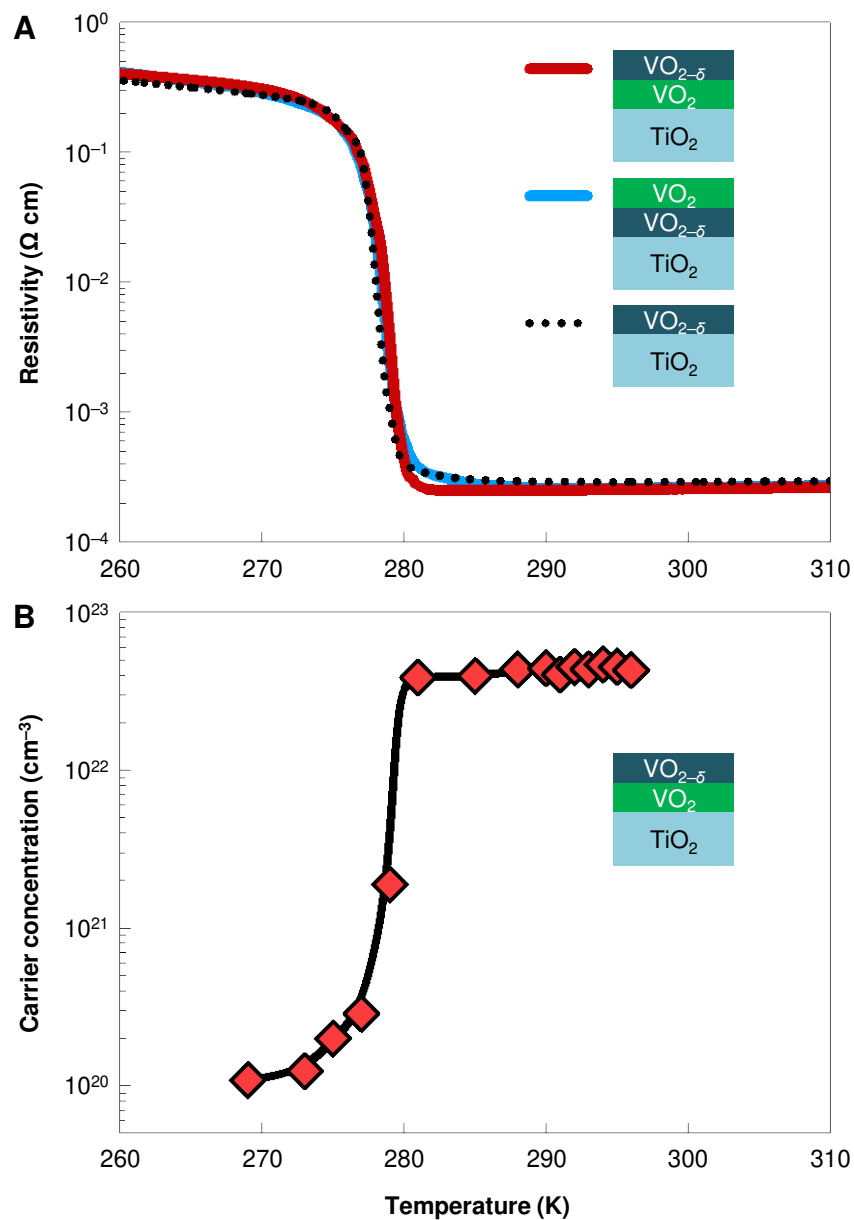


Fig. S7. Transport measurement. (A) Electrical resistivity as a function of temperature on cooling for $\text{VO}_{2-\delta}$ (8 nm)/ VO_2 (8 nm) bilayer (red line), VO_2 (8 nm)/ $\text{VO}_{2-\delta}$ (8 nm) bilayer (blue line), and 8-nm-thick $\text{VO}_{2-\delta}$ single layer (black dotted line). (B) Carrier concentration as a function of temperature on cooling for $\text{VO}_{2-\delta}$ (8 nm)/ VO_2 (8 nm) bilayer. Black solid line is the guide to eyes.

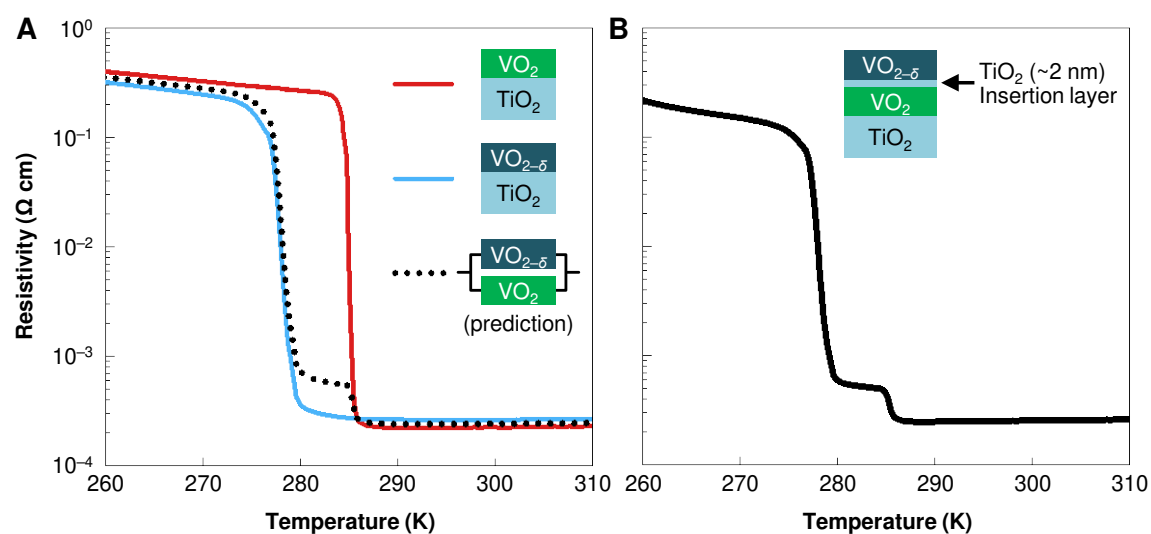


Fig. S8. Metal-insulator transition of the trilayer. (A) Predicted metal-insulator transition on cooling for the simply parallel-connected 8-nm-thick VO_2 and 8-nm-thick $\text{VO}_{2-\delta}$ layers without any interfacial interaction. (B) Measured metal-insulator transition on cooling for the $\text{VO}_{2-\delta}$ (8 nm)/ TiO_2 (2 nm)/ VO_2 (8 nm) trilayer.

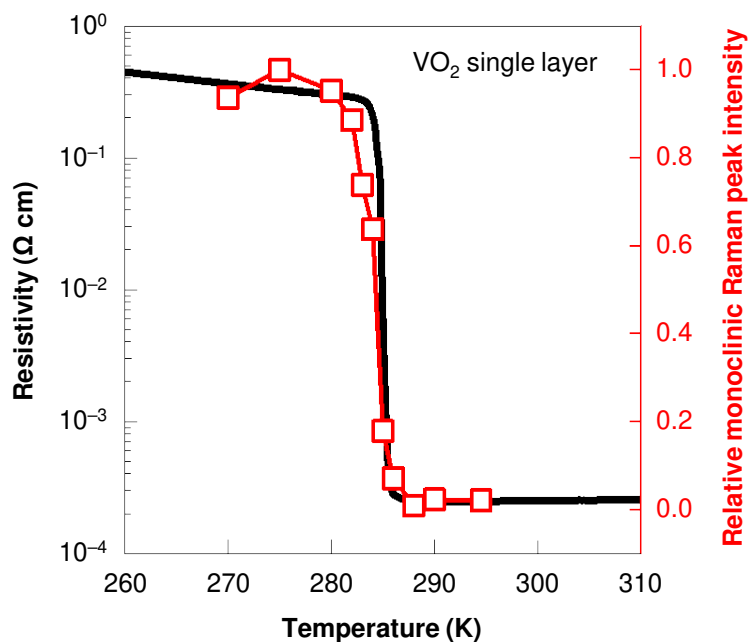


Fig. S9. Metal-insulator and structural phase transitions of VO₂ single layer. Metal-insulator and structural phase transitions, measured on cooling in VO₂ single layer, show a single-step feature.

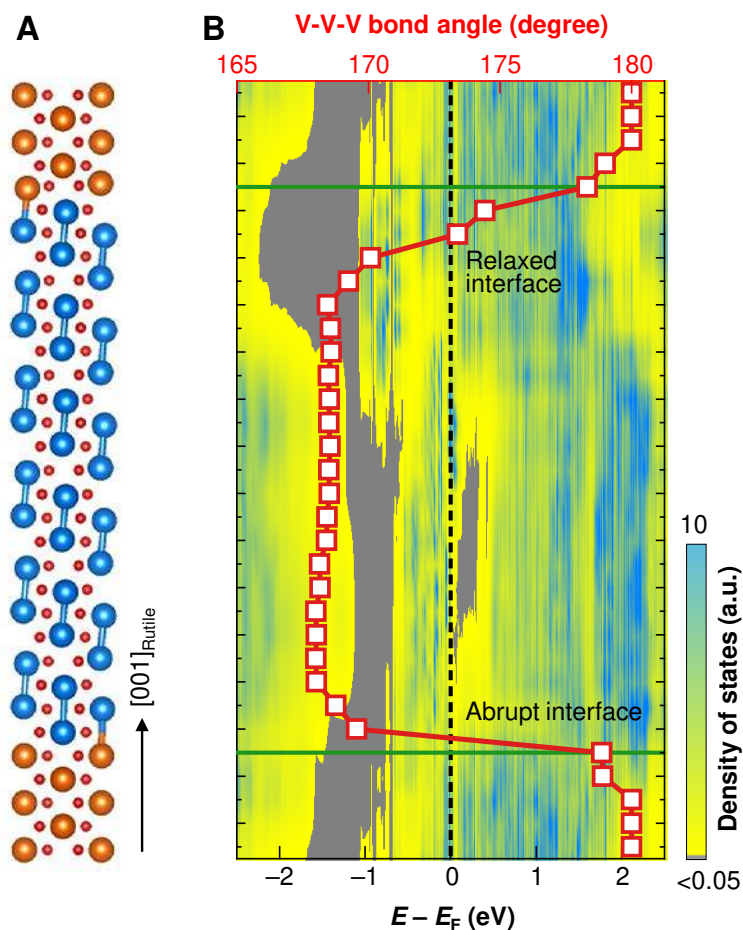


Fig. S10. Calculated electronic structure of the rutile/monoclinic heterostructure. (A) Calculated atomic structure for 6-unit-cells (including 23 planes of VO₂) of monoclinic VO₂, sandwiched by rutile VO₂. While we fixed the atomic positions of two-unit-cell monoclinic region near the lower interface as bulk-like, we allowed full atomic relaxation in all other monoclinic regions. (B) Calculated density of states for each layer as a function of energy $E - E_F$. Gray color indicates the regions that have the density of states, lower than 0.05. We also represent the values of V-V-V bond angle along the [001]_{Rutile} axis, an indication of monoclinic distortion, for each layer by open red squares.

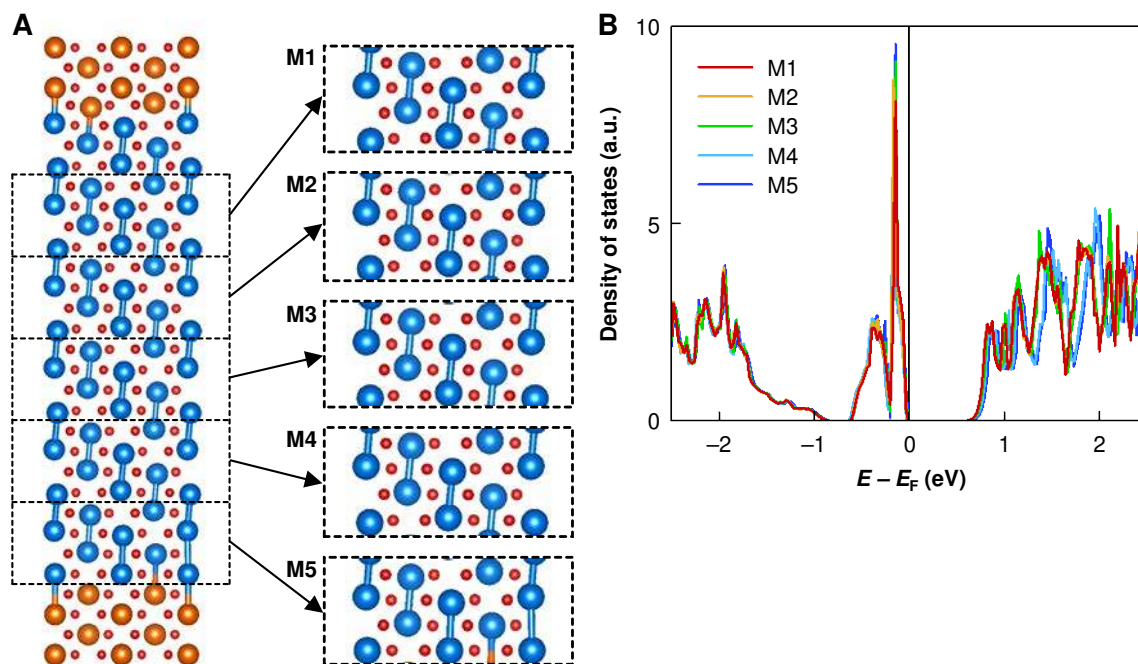


Fig. S11. Density-of-states calculation for the captured local monoclinic structure. (A) We captured a local monoclinic structure (denoted by M1, M2, M3, M4, and M5) in the rutile/monoclinic superlattice, and then used it as a bulk structure for the density of states calculation. (B) Calculated density of states for a bulk monoclinic employing the captured local monoclinic structures.

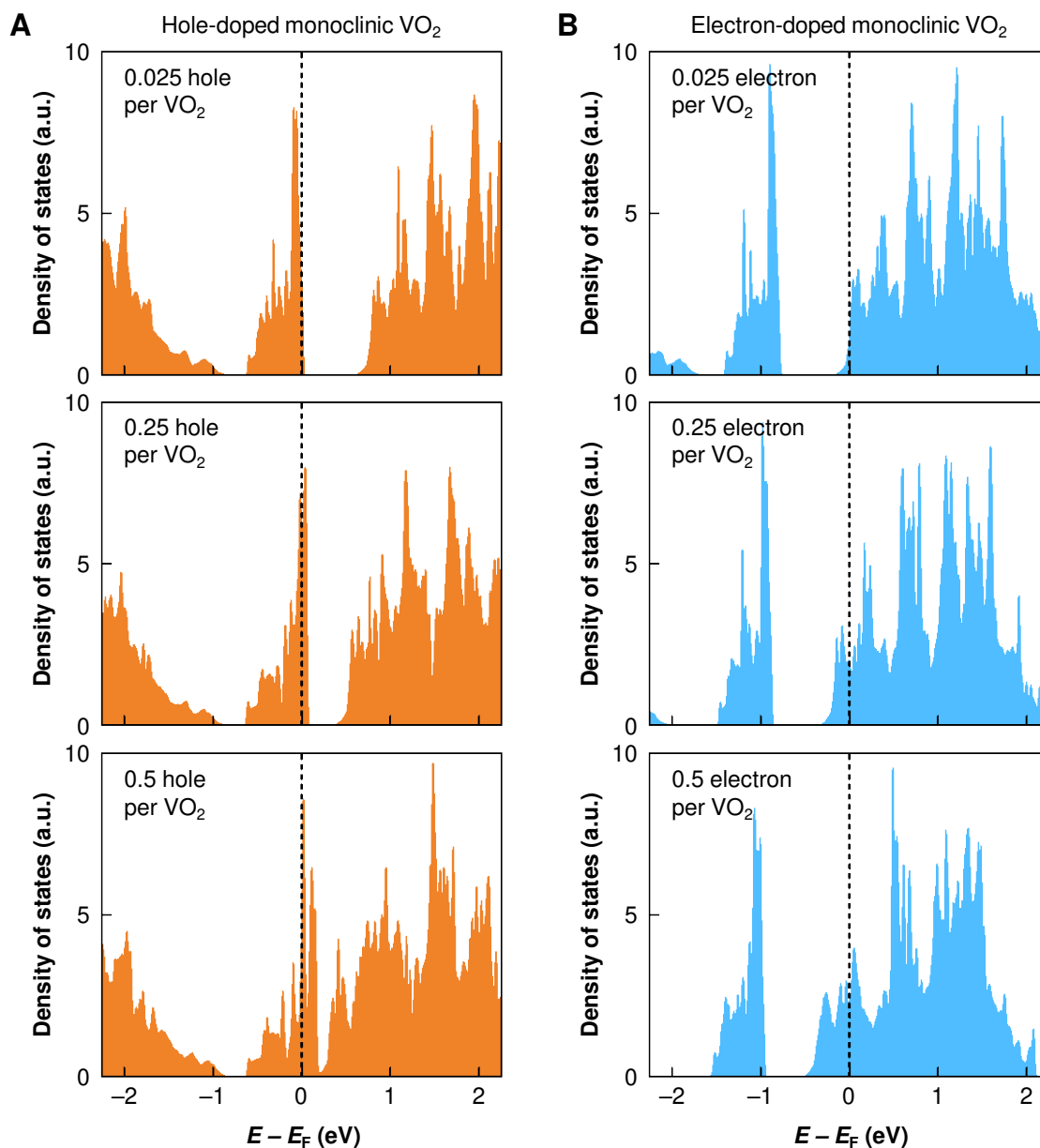


Fig. S12. Calculated electronic structure of hole- and electron-doped monoclinic VO_2 . (A) Calculated density of states of hole-doped monoclinic VO_2 , which show a significant band-gap narrowing with increasing the hole concentration. (B) Calculated density of states of electron-doped monoclinic VO_2 , which show a negligible band-gap narrowing with increasing the electron concentration.

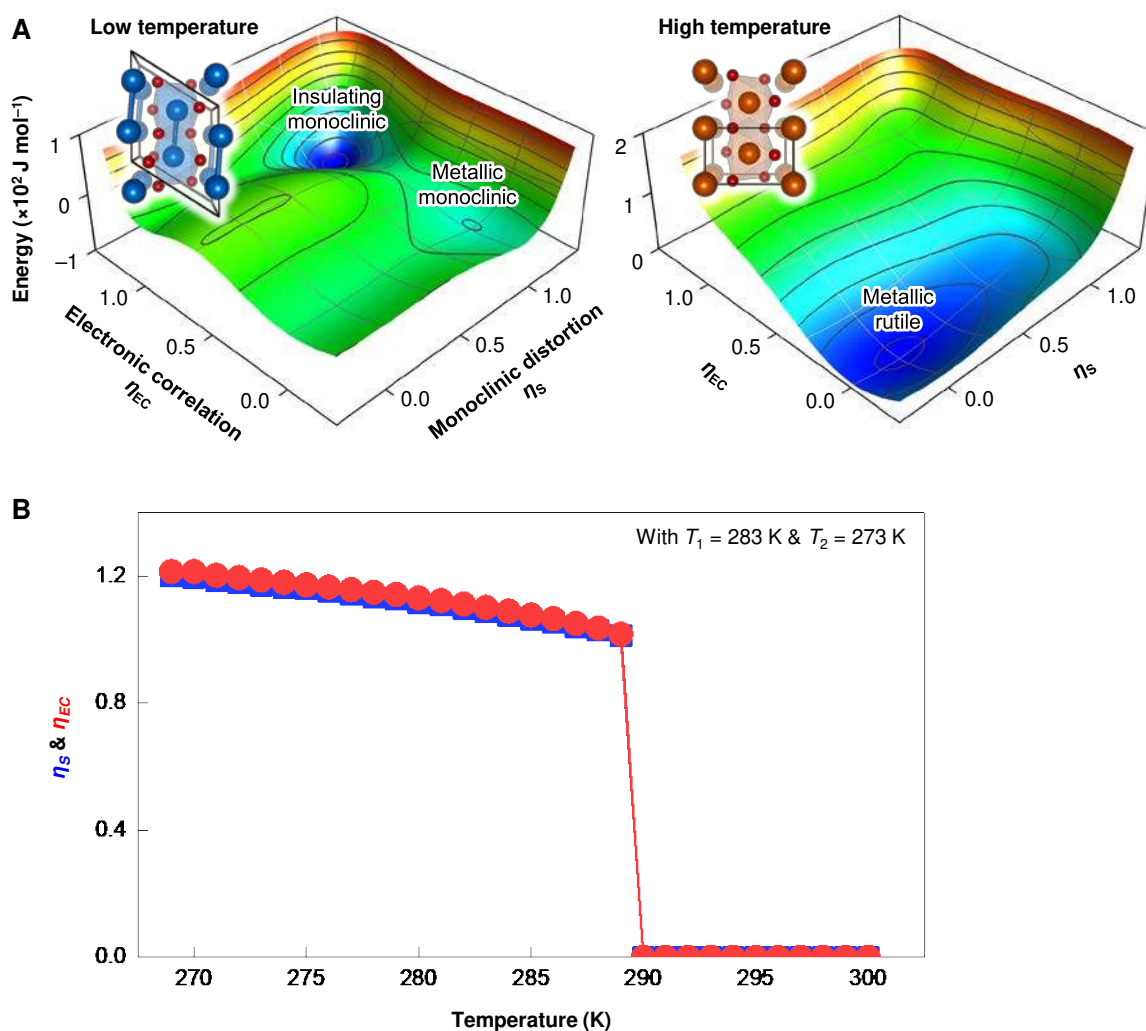


Fig. S13. Simulated phase transitions in bulk VO₂. (A) Free energy landscape of bulk VO₂ at 287 K (left) and 292 K (right). (B) Temperature dependence of η_S and η_{EC} , which make the global minimum in free energy (i.e., equilibrium phase) at each temperature.

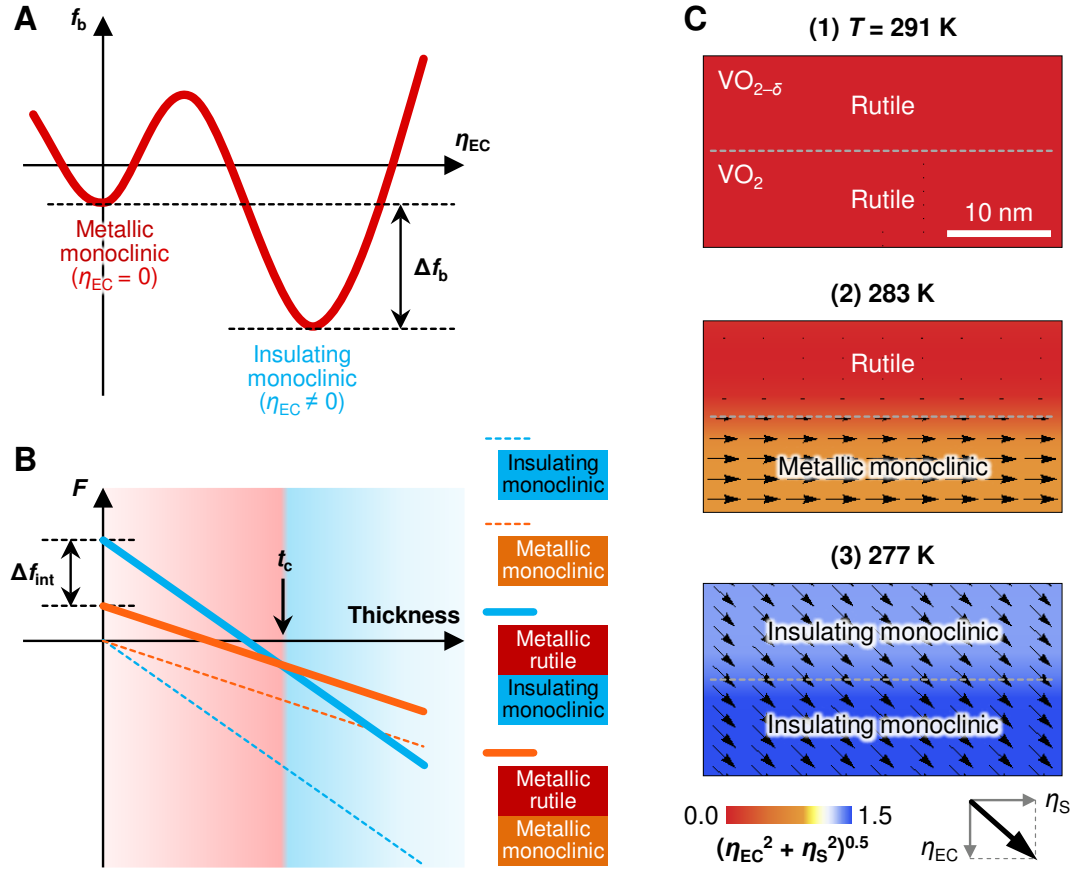


Fig. S14. Emergence of stable metallic monoclinic phase. (A) A schematic of bulk molar Landau potential, showing the non-equilibrium (metastable) metallic monoclinic phase, as well as equilibrium (stable) insulating monoclinic phase. (B) A schematic of total energy per area as a function of thickness in the rutile/monoclinic heterostructure. (C) Stable states, calculated by phase-field simulations, of the $VO_{2-\delta}/VO_2$ bilayer for temperatures of $T = 291$ K, 283 K, and 277 K. The arrows represent the two-component order parameter (η_s, η_{EC}) , and the color represents the norm $(\eta_s^2 + \eta_{EC}^2)^{0.5}$. Thickness of each layer is set to be below $t_c \sim 9.4$ nm.

Table S1.

The values of Landau coefficients we use.

a_1	b_1	c_1	T_{EC}	a_2	b_2
8626 J/mol	-1675 J/mol	1294 J/mol	273 K	5176 J/mol	-668.3 J/mol
c_2	T_S	g_1	g_2	k_1	k_2
696.5 J/mol	283 K	0.8625 J/mol	155.3 J/mol	0.40 eV/nm	0.16 eV/nm